Article

Cell

DNA Damage Signaling Instructs Polyploid Macrophage Fate in Granulomas

Graphical Abstract

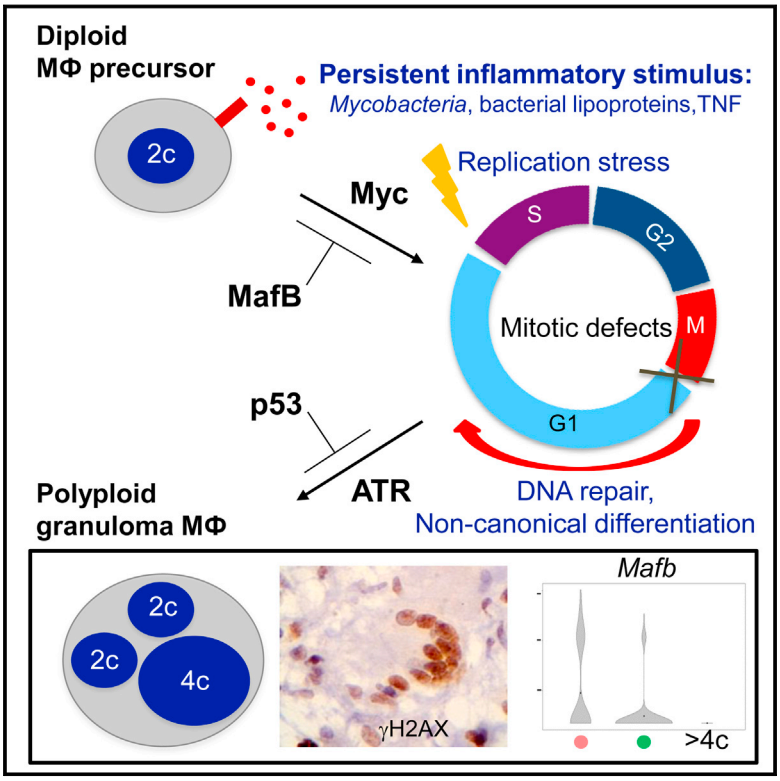

Highlights

- Polyploid macrophage fate is controlled by persistent inflammatory stimuli
- Polyploid granuloma macrophages form by modified cell divisions and mitotic defects
- Polyploid macrophages grow by overcoming p53-dependent barriers to their proliferation
- Myc and the DNA Damage Response promote polyploid macrophage differentiation

Authors

Laura Herrtwich, Indrajit Nanda, Konstantinos Evangelou, ..., Andreas Diefenbach, Philipp Henneke, Antigoni Triantafyllopoulou

Correspondence

diefenbach@uni-mainz.de (A.D.), antigoni.triantafyllopoulou@uniklinik-freiburg.de (A.T.)

In Brief

Polyploid macrophages develop in response to chronic inflammatory signaling from toll-like receptors via replication stress and activation of the DNA damage response.

Herrtwich et al., 2016, Cell *167*, 1264–1280
November 17, 2016
http://dx.doi.org/10.1016/j.cell.2016.09.054

CellPress

Cell

Article

DNA Damage Signaling Instructs Polyploid Macrophage Fate in Granulomas

Laura Herrtwich,[1,2,29] Indrajit Nanda,[3,29] Konstantinos Evangelou,[4,29] Teodora Nikolova,[5,29] Veronika Horn,[1,29] Sagar,[6] Daniel Erny,[7] Jonathan Stefanowski,[8] Leif Rogell,[6,9,10] Claudius Klein,[11] Kourosh Gharun,[2] Marie Follo,[11] Maximilian Seidl,[12] Bernhard Kremer,[2] Nikolas Münke,[2] Julia Senges,[2] Manfred Fliegauf,[2] Tom Aschman,[1] Dietmar Pfeifer,[11] Sandrine Sarrazin,[13] Michael H. Sieweke,[13,14] Dirk Wagner,[2,15] Christine Dierks,[11]

(Author list continued on next page)

[1]Department of Rheumatology and Clinical Immunology, Medical Center – University of Freiburg, Faculty of Medicine, University of Freiburg, 79106 Freiburg, Germany
[2]Center of Chronic Immunodeficiency, Medical Center – University of Freiburg, Faculty of Medicine, University of Freiburg, 79106 Freiburg, Germany
[3]Institute of Human Genetics, Biozentrum, Am Hubland, 97074 Würzburg, Germany
[4]Molecular Carcinogenesis Group, Department of Histology and Embryology, School of Medicine, National and Kapodistrian University of Athens, 115 27 Athens, Greece
[5]Institute of Toxicology, University Medical Center Mainz, 55131 Mainz, Germany
[6]Max Planck Institute of Immunobiology and Epigenetics, 79108 Freiburg, Germany
[7]Institute of Neuropathology, Medical Center, University of Freiburg, Faculty of Medicine, University of Freiburg, 79106 Freiburg, Germany
[8]Immune Dynamics, Charité Universitätsmedizin and Deutsches Rheumaforschungszentrum, 10117 Berlin, Germany
[9]Institute of Medical Microbiology and Hygiene, University of Mainz Medical Center, 55131 Mainz, Germany
[10]Research Center for Immunology and Immunotherapy, University of Mainz Medical Center, 55131 Mainz, Germany
[11]Department of Medicine I, Medical Center, University of Freiburg, Faculty of Medicine, University of Freiburg, 79106 Freiburg, Germany
[12]Department of Pathology, Medical Center, University of Freiburg, Faculty of Medicine, University of Freiburg, 79106 Freiburg, Germany
[13]Aix-Marseille Univ, CNRS, INSERM, CIML, 13288 Marseille, France
[14]Max-Delbrück-Centrum für Molekulare Medizin in der Helmholtzgemeinschaft (MDC), 13125 Berlin, Germany
[15]Division of Infectious Diseases, Department of Internal Medicine 2, Medical Center – University of Freiburg, Faculty of Medicine, University of Freiburg, 79106 Freiburg, Germany
[16]Eye Center, Medical Center – University of Freiburg, Faculty of Medicine, University of Freiburg, 79106 Freiburg, Germany
[17]Department of Internal Medicine 3, Rheumatology and Immunology, University of Erlangen-Nuremberg, 91054 Erlangen, Germany
[18]Center for Sepsis Control and Care, Jena University Hospital, 07747 Jena, Germany
[19]BIOSS Centre for Biological Signalling Studies, University of Freiburg, 79106 Freiburg, Germany
[20]Department of Pathology, Schleswig-Holstein University Hospital, Campus Lübeck and Research Center Borstel, 23845 Borstel, Germany
[21]Division of Infection Immunology, Research Center Borstel, 23845 Borstel, Germany
[22]Cluster of Excellence, Inflammation at Interfaces (Borstel-Kiel-Lübeck-Plön), 24118 Kiel, Germany

(Affiliations continued on next page)

SUMMARY

Granulomas are immune cell aggregates formed in response to persistent inflammatory stimuli. Granuloma macrophage subsets are diverse and carry varying copy numbers of their genomic information. The molecular programs that control the differentiation of such macrophage populations in response to a chronic stimulus, though critical for disease outcome, have not been defined. Here, we delineate a macrophage differentiation pathway by which a persistent Toll-like receptor (TLR) 2 signal instructs polyploid macrophage fate by inducing replication stress and activating the DNA damage response. Polyploid granuloma-resident macrophages formed via modified cell divisions and mitotic defects and not, as previously thought, by cell-to-cell fusion. TLR2 signaling promoted macrophage polyploidy and suppressed genomic instability by regulating Myc and ATR. We propose that, in the presence of persistent inflammatory stimuli, pathways previously linked to oncogene-initiated carcinogenesis instruct a long-lived granuloma-resident macrophage differentiation program that regulates granulomatous tissue remodeling.

INTRODUCTION

Granulomatous diseases of infectious, autoinflammatory, allergic, and malignant etiologies, such as mycobacterial disease, vasculitis, inflammatory bowel disease, and sarcoidosis affect millions of people worldwide. Their common hallmark is

Thomas Haaf,[3] Thomas Ness,[16] Mario M. Zaiss,[17] Reinhard E. Voll,[1] Sachin D. Deshmukh,[18] Marco Prinz,[7,19] Torsten Goldmann,[20] Christoph Hölscher,[21,22,23] Anja E. Hauser,[8] Andres J. Lopez-Contreras,[24] Dominic Grün,[6] Vassilis Gorgoulis,[4,25,26,27] Andreas Diefenbach,[9,10,*] Philipp Henneke,[2,28] and Antigoni Triantafyllopoulou[1,2,30,*]
[23]German Centre for Infection Research, 23845 Borstel, Germany
[24]Center for Chromosome Stability, Department of Cellular and Molecular Medicine, Panum Institute, University of Copenhagen, 2200 Copenhagen N, Denmark
[25]Faculty Institute of Cancer Sciences, Manchester Academic Health Sciences Centre, University of Manchester, Manchester M20 4QL, UK
[26]Biomedical Research Foundation, Academy of Athens, 115 27 Athens, Greece
[27]Department of Pathophysiology School of Medicine, National and Kapodistrian University of Athens, 115 27 Athens, Greece
[28]Center for Pediatrics and Adolescent Medicine, Medical Center, University of Freiburg, Faculty of Medicine, University of Freiburg, 79106 Freiburg, Germany
[29]Co-first author
[30]Lead Contact
*Correspondence: diefenbach@uni-mainz.de (A.D.), antigoni.triantafyllopoulou@uniklinik-freiburg.de (A.T.)
http://dx.doi.org/10.1016/j.cell.2016.09.054

formation of a granuloma, a compact and often highly ordered aggregate of immune cells that forms in response to a persistent inflammatory stimulus. At its core, the granuloma consists of different macrophage (MΦ) subsets displaying a range of morphologies, such as epithelioid MΦ, foam cells (i.e., MΦ loaded with lipid droplets), mononuclear (MoNucl), binuclear (BiNucl), and multinuclear (MultiNucl) MΦ (or MMΦ), and *Langhans* giant cells (Ramakrishnan, 2012; Williams and Williams, 1983). The molecular programs that control the differentiation of such MΦ populations in response to a chronic stimulus are likely critical to disease outcome. A prominent example is tuberculosis, a pandemic infectious disease caused by *Mycobacterium (M.) tuberculosis*. *M. tuberculosis* infects approximately a third of the world's population and is the leading cause of death from a bacterial infection worldwide (Nathan, 2009). In tuberculosis, distinct spectra of MΦ differentiation determine disease outcome. On one end of the spectrum, microbicidal MΦ kill intracellular bacteria. On the other end, permissive MΦ provide mycobacteria with a replicative niche. These spectra are characterized by distinct metabolic and effector profiles. Thus, microbicidal MΦ produce reactive nitrogen species, MΦ characterized by lipid accumulation (foam cells) are associated with granuloma necrosis and bacterial persistence (Peyron et al., 2008; Russell et al., 2009), and MΦ expressing extracellular matrix (ECM)-remodeling molecules, such as matrix metalloproteinase 9 (MMP9) are crucial for granuloma formation and bacterial spread (Taylor et al., 2006; Volkman et al., 2010). It is currently unknown if the various phenotypically distinct MΦ subsets contained in granulomas exhibit distinct metabolic or functional profiles. Thus, the mechanisms controlling MΦ differentiation and the functional profiles of the various MΦ subsets contained in granulomas are key to identifying novel strategies to promote host resistance.

Within the scope of understanding MΦ cell-fate decisions in granulomas, an important and unresolved question relates to MΦ polyploidization. It is generally believed that the formation of polyploid giant cells can be explained by cell-to-cell fusion (Helming and Gordon, 2009). While this has been well documented for RANKL-induced osteoclasts and for the generation of MMΦ using stimulation of non-cycling progenitors with mycobacteria or bacterial lipoproteins (BLPs) in vitro (Puissegur et al., 2007), direct evidence for cell-to-cell fusion as the leading process for the genesis of the various polyploid MΦ subsets found in granulomatous diseases is lacking. The fact that MΦ in granulomas carry varying copy numbers of their genomic information poses a series of significant basic questions that have not been addressed to date. Does the formation of polyploid MΦ pose a threat to their genomic stability? What is the role of the DNA damage response in MΦ differentiation into polyploid subsets? Do polyploid MΦ constitute a distinct fate that contributes to the pathogenesis of granulomatous diseases?

Here, using an array of techniques, we delineate a MΦ differentiation pathway in response to persistent inflammatory stimuli. Sensing of BLP controlled the differentiation of proliferating MΦ precursors into polyploid MΦ expressing distinct metabolic and ECM remodeling gene expression signatures. Toll-like receptor (TLR)2 signaling via MyD88 promoted MΦ genome duplications via mitotic defects but not by cell-to-cell fusion. BLP-induced polyploid MΦ grew further by re-entering the cell cycle and overcoming p53-dependent barriers to their proliferation. TLR2 signaling promoted MΦ polyploidy and alleviated genomic instability, by regulating Myc and the DNA damage response (DDR). Therefore, we have unlocked a previously unknown and unique role of growth and DDR signals in determining MΦ differentiation in the presence of persisting inflammatory stimuli.

RESULTS

MΦ with Varying Numbers of Nuclei Co-localize with Proliferating F4/80$^+$ Precursors in Small Mycobacterial Granulomas

To identify mechanisms by which persistent inflammatory signals instruct MΦ differentiation in granulomas, we used infection with *M. bovis* Bacillus Calmette-Guerin (BCG). BCG induced the formation of BiNucl MΦ and MMΦ in liver granulomas (Figures S1A–S1B) and increased the numbers of proliferating (Ki67$^+$) F4/80$^+$ cells (Figures S1C and S1D). In smaller granulomas, an organized topographical arrangement of Ki67$^+$F4/80$^+$ precursors and BiNucl MΦ or MMΦ emerged: the former were positioned in the outside (Figure S1E), while BiNucl MΦ and MMΦ were found primarily in the center of the granuloma (Figure S1F). In more mature granulomas, Ki67$^+$F4/80$^+$ cells were fewer and their location within granulomas was ill defined (Figure S1G). These data raised the possibility that during BCG infection

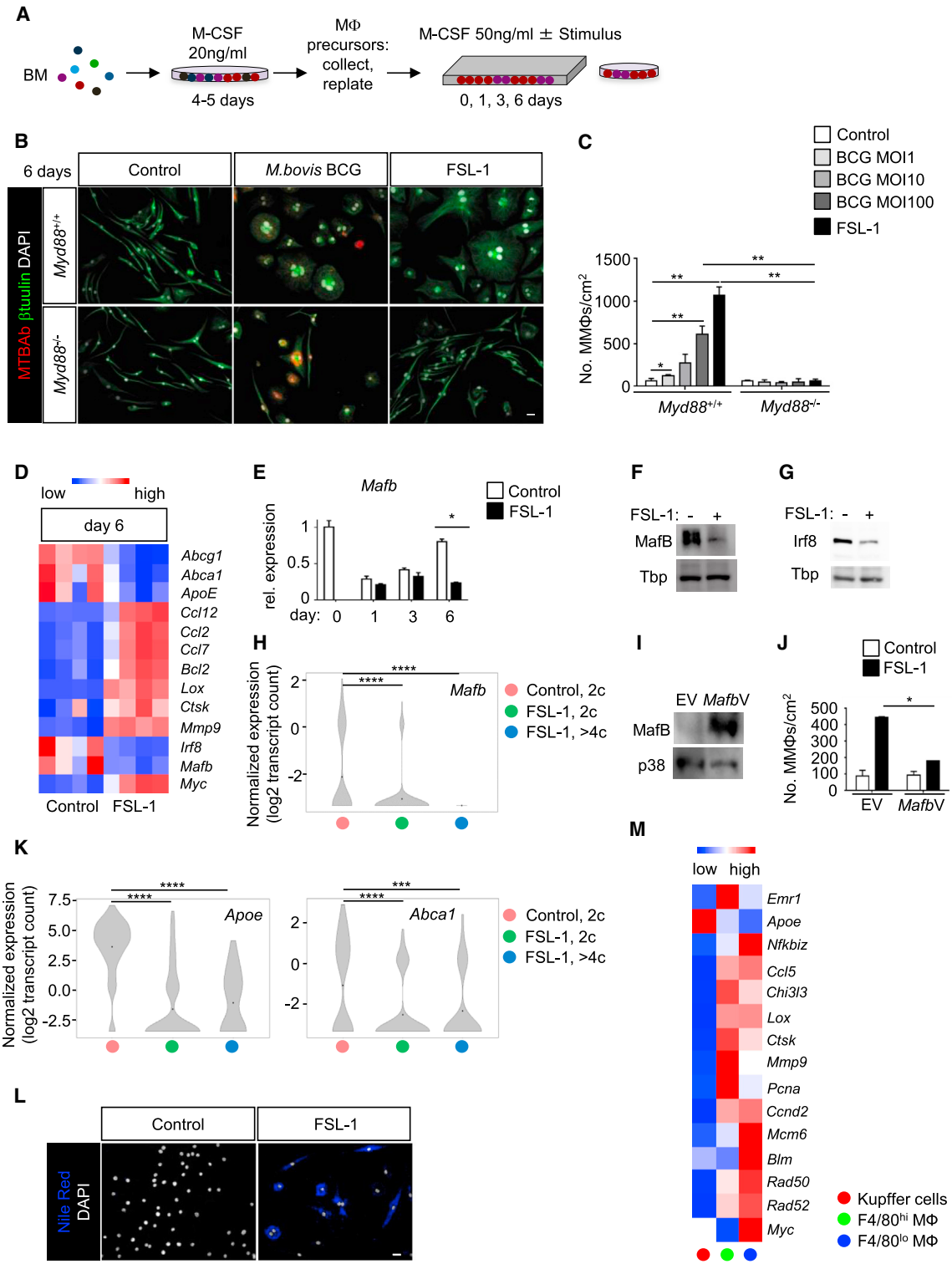

Figure 1. BLPs Mediate Non-canonical MΦ Differentiation

(A) Experimental setup for differentiation of MMΦ using proliferating MΦ precursors.

(B) Examples of MMΦ.

(C) Numbers of MMΦ. Mean ± SD from three independent experiments.

(D) Heatmap of differentially expressed genes, selected based on involvement in MΦ function or differentiation programs. Gene array was performed with four independent biological replicates per group.

(legend continued on next page)

proliferating precursor cells differentiate into MΦ with varying numbers of nuclei and potentially varying copy numbers of their genome.

TLR2 and MyD88-Dependent Differentiation of MΦ Precursors into MMΦ

To explore the molecular programs that drive the differentiation of MΦ precursors into polyploid MΦ, we compared the ability of uncommitted hematopoietic progenitors, common MΦ dendritic cell progenitors (MDPs), and mature monocytes to differentiate into MMΦ following stimulation with M-CSF and FSL-1 (a synthetic BLP acting as a ligand for the TLR2/6 complex) (Figure S1H). Intriguingly, only MDP formed numerous large MMΦ (Figures S1I–S1J). Similar to MDP, CD115^{high} MΦ precursors (Figure S1K), enriched by culturing bone marrow (BM) cells first for 4–5 days in low concentrations of M-CSF and then reseeded and stimulated with BCG or FSL-1, differentiated very efficiently into MMΦ (Figures 1A and 1B), a process that required signaling via the adaptor protein MyD88 (Figures 1B and 1C). MMΦ started to form after 3 days, and their numbers continuously increased until day 6 of stimulation (Figure S2A). When such CD115^{high} MMΦ precursors were cultured with M-CSF alone, they uniformly differentiated into conventional BM-derived MΦ (Figure 1B). These data indicated that the cycling capacity and differentiation potential of precursor cells may be an essential determinant of their ability to form MultiNucl progeny in response to BLP.

Ligands of TLR2/1 (Pam3CSK4) and TLR2/6 (FSL-1) receptor complexes were more efficient in inducing differentiation of MMΦ than the TLR4 ligand LPS (Figure S2B). Poly(I:C), which signals via TLR3, RIG-I, and MDA5, did not induce MMΦ formation (Figure S2B). We asked whether cytokines that are known to be crucial for granuloma formation can induce MMΦ. Tumor necrosis factor (TNF) induced differentiation of MMΦ as efficiently as FSL-1 (Figure S2C), but interferon (IFN)-γ and interleukin (IL)-1β did not (Figure S2D). Do BLPs induce MMΦ indirectly by inducing a secreted cytokine, such as TNF? To this end, we mixed CD45.1^{+}*Myd88*$^{+/+}$ with congenic CD45.2^{+}*Myd88*$^{-/-}$ MΦ precursors in vitro prior to stimulation with FSL-1 (Figures S2E and S2F). Within the same well, only CD45.1^{+}*Myd88*$^{+/+}$ cells formed MMΦ, whereas CD45.2^{+}*Myd88*$^{-/-}$ cells did not, demonstrating that cell-autonomous MyD88 signaling was required for BLP-induced MMΦ formation (Figures S2E and S2F). In addition, *Tnf*$^{-/-}$ MΦ precursors were not impaired in forming MMΦ when stimulated with FSL-1 (Figures S2G and S2H). These data indicated that TLR2 and TNF pathways can independently instruct MMΦ fate.

A Non-canonical MΦ Differentiation Program Instructs Polyploid MΦ Fate

MMΦ contain several nuclei and clearly display a distinct morphology (Figure 1B), suggesting that BLPs induce a non-canonical MΦ differentiation program, which differs from that induced by M-CSF stimulation alone. To explore this, we performed genome-wide transcriptome analysis of MΦ precursors with and without stimulation with BLP. When comparing gene expression signatures of MΦ precursors stimulated with M-CSF and those stimulated with M-CSF and BLP, we found a significant downregulation of MΦ cell-fate-determining transcription factors (Geissmann et al., 2010), including *Mafb* and *Irf8* (Figure 1D), which was confirmed by qRT-PCR and immunoblot (IB) (Figures 1E–1G).

Since only a fraction of cells are MMΦ after culture in FSL-1, we performed single-cell (sc) RNA sequencing (RNA-seq) on highly purified FSL-1-stimulated cells with a DNA content of 2c (F2c), >4c (F>4c), and control 2c MΦ (Ctrl) (Figures S3A and S3B). scRNA-seq analysis using the RaceID2 algorithm (Grün et al., 2016) revealed considerable heterogeneity among Ctrl MΦ, but also among F2c and F>4c MΦ (Figures S3C and S3D). Differential gene expression analysis within each of these groups identified a number of genes differentially expressed between F2c and F>4c MΦ (e.g., *Cdk1*, *Tubb5*, *Actg1*, *Mmp9*) (Figure S3E). Moreover, *Apoe* and *Csf1r* were further downregulated in F>4c compared to F2c MΦ in clusters 5 and 9, respectively (Figure S3E). These findings indicate that, although F>4c MΦ cluster together with F2c MΦ based on whole-transcriptome similarity, they exhibit additional expression changes of various MMΦ differentiation signature genes indicative of their advanced stage of differentiation. The presence of F>4c MΦ in different clusters also suggests the existence of multiple differentiation endpoints after FSL-1 stimulation.

While MΦ differentiated in M-CSF alone expressed robust levels of *Mafb*, *Mafb* expression was abruptly shut down in F>4c, and *Mafb* was already downregulated in F2c MΦ (Figure 1H). Enforced expression of MafB in MΦ precursors suppressed the formation of MMΦ (Figures 1I and 1J). These data suggest that MΦ precursor differentiation into MMΦ has transcriptional requirements that are distinct from canonical MΦ differentiation and may represent a distinct differentiation program driven by a persisting inflammatory stimulus.

Metabolic and Tissue-Remodeling Gene Signatures of MMΦ

Next, we assessed transcripts that differed at least 2-fold between FSL1-stimulated MΦ and controls. FSL1-stimulated MΦ

(E–J) MafB negatively regulates MMΦ formation. (E) qRT-PCR of *Mafb* mRNA expression. Mean ± SD of triplicate determinants from three independent experiments. (F and G) Immunoblotting (IB) for MafB and IRF8. Example of two independent experiments. (H) Violin plots comparing expression of *Mafb*, by scRNA-seq. (I and J) MΦ precursors transduced with empty retroviral vector pMX-IRES-*EGFP* (EV) or pMX-*Mafb*-IRES-*EGFP* (*Mafb*V) prior to stimulation. (I) IB for MafB. (J) Numbers of MMΦs. Mean ± SD from three independent experiments.

(K and L) Metabolic gene signatures in BLP-induced MMΦ. (K) Violin plots comparing expression of *Apoe*; *Abca1* was analyzed by scRNA-seq. (L) IF for Nile Red is shown.

(M) Heatmap of selected genes differentially expressed in Kupffer cells, granuloma F4/80^{hi} MΦ, and F4/80^{low} BiNucl and MMΦ. Means of duplicate determinants from five to nine independent biological replicates per group.

(E and M) qRT-PCR data normalized relative to *Gapdh* mRNA expression.

(H and K) y axis, log2 (normalized count+0.1) expression levels; black point, mean of expression level.

*$p < 0.05$, **$p < 0.01$; scale bars, 10 μm. See also Figures S1, S2, S3, and S4.

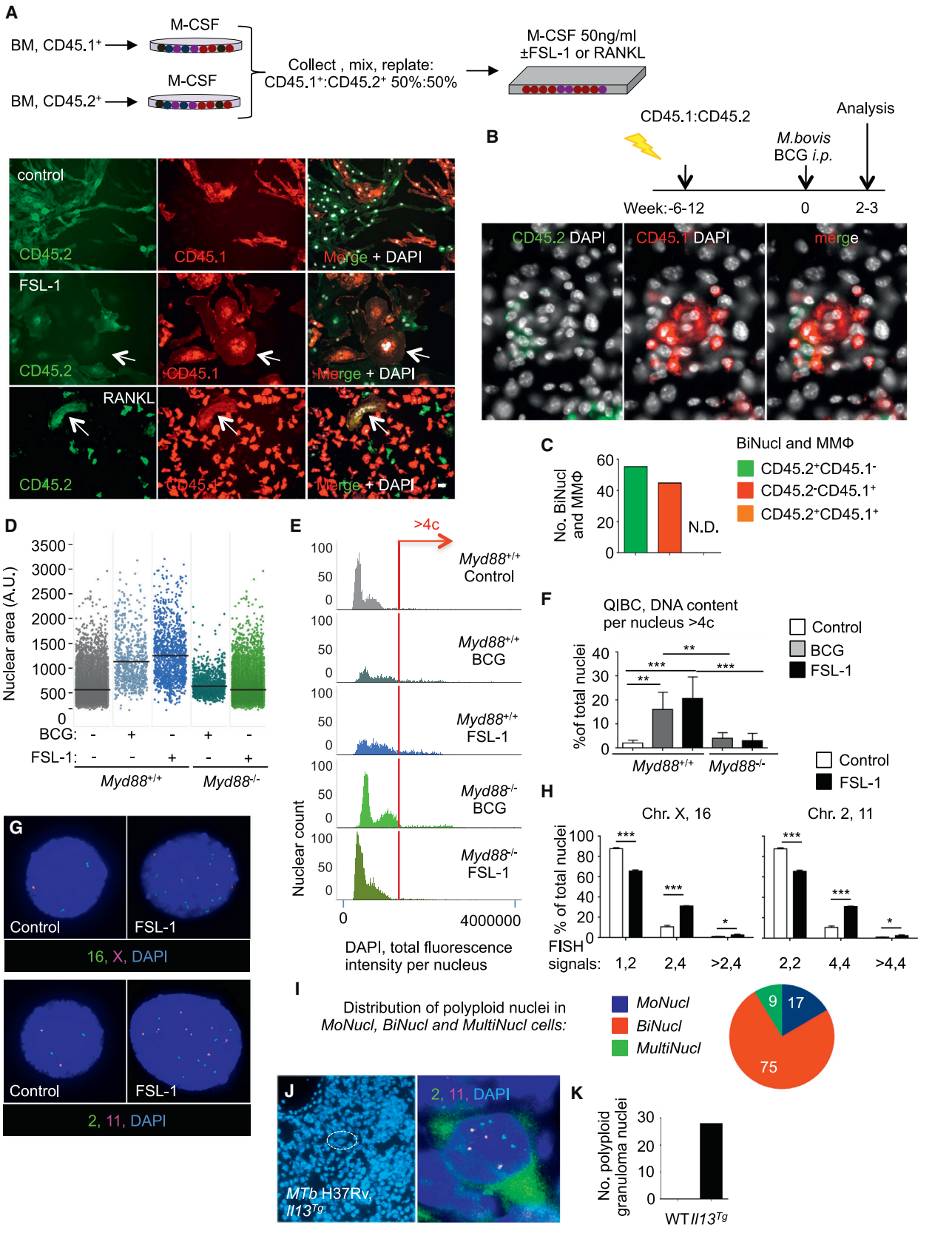

(legend on next page)

significantly downregulated expression of genes regulating cholesterol efflux, such as *Abcg*, *Abca*, and *Apoe* (Figure 1D), which was verified by scRNA-seq (Figure 1K). Reactome pathway analysis revealed that F2c MΦ were highly enriched in genes involved in cholesterol biosynthesis while F>4c MΦ downregulate lipid metabolizing gene signatures (Figure S4). Accordingly, Nile Red immunofluorescence (IF) revealed lipid body accumulation in FSL-1-stimulated MoNucl MΦ and MMΦ (Figure 1L), indicating that the BLP-controlled MMΦ differentiation program leads to functional changes in cholesterol metabolism.

In FSL1-stimulated MΦ, transcripts for MΦ-attracting chemokines (i.e., *Ccl2*, *Ccl7*, and *Ccl12*) were 7- to 12-fold upregulated (Figure 1D). scRNA-seq revealed that these chemokines are already upregulated in F2c and remain highly expressed in F > 4c MΦ (Figure S3F). BLPs induced increased expression of genes encoding for ECM remodeling proteases, such as *Mmp8*, *Mmp9*, *Chi3l3*, *Ctsk*, and *Lox* (Figures 1D and S3F), and ECM remodeling gene pathways were highly enriched in both F2c and F>4c MΦ (Figure S3E, cluster 13, and Figure S4). This is an intriguing finding because ECM remodeling enzymes such as MMP9 are crucial for MΦ recruitment and granuloma formation (Taylor et al., 2006; Volkman et al., 2010).

Finally, we used laser capture microdissection (LCM) to isolate F4/80^{hi} MΦ and F4/80^{low} BiNucl and MMΦ from BCG liver granulomas and control liver-resident MΦ to confirm that the gene signatures observed in vitro can also be found in MMΦ from mycobacterial granulomas in vivo. qRT-PCR-based quantification of selected transcripts revealed that cholesterol transporters were downregulated, whereas genes associated with ECM remodeling were strongly upregulated in MMΦ directly isolated from mycobacterial granuloma (Figures 1M and S3G–S3I). Thus, MMΦ differentiating in the presence of a persistent TLR2 stimulus show alterations in cholesterol and lipid metabolism and ECM remodeling gene expression signatures.

MMΦ Form by a Mechanism Distinct from Cell-to-Cell Fusion

We attempted to quantify cell-to-cell fusion by mixing CD45.1$^+$ with congenic CD45.2$^+$ MΦ precursors, followed by stimulation with BLP (Figure 2A). As a positive control, we used RANKL, a cytokine known to induce osteoclast formation by cell-to-cell fusion (Vignery, 2005). While RANKL-stimulated MΦ precursors differentiated into MultiNucl osteoclast-like CD45.1$^+$ CD45.2$^+$ cells indicating cell-to-cell fusion, BLP stimulation did not lead to the generation of MMΦ co-expressing CD45.1 and CD45.2 (Figure 2A). To explore whether fusion may occur in vivo, we generated mixed BM chimeras by transplanting lethally irradiated CD45.2$^+$ mice with a mixture of BM cells obtained from CD45.1$^+$ and CD45.2$^+$ donors (Figure S5A). BM chimeric mice were infected with BCG (Figure 2B) and, if the cell-to-cell fusion paradigm was true, we expected roughly 50% of polyploid MΦ to co-express CD45.1 and CD45.2. However, we did not identify any BiNucl MΦ or MMΦ that expressed both CD45.1 and CD45.2 in BCG granulomas (Figures 2B, 2C, and S5B). As a control for our staining procedure, we employed BM from (CD45.1xCD45.2) F1 mice, leukocytes of which were double positive for CD45.1 and CD45.2. Thus, IF staining for CD45.1 and CD45.2 faithfully detects double positive cells, if they exist (Figure S5C). These data demonstrate that differentiation of MMΦ in the presence of a persistent inflammatory stimulus occurs by a previously unappreciated process that does not involve cell-to-cell fusion.

Persistent Exposure to BLP Regulates MΦ Ploidy via Modified Cell Division

In mammalian cells, other than MΦ, polyploidization via modified cell division has been described (i.e., endoreplication, cytokinesis failure) (Figures S5D and S5E) (Davoli et al., 2010). To explore this possibility, we analyzed the nuclear area and nuclear DNA content of single nuclei in an unbiased, high-content fashion using a quantitative image-based cytometry (QIBC) protocol, allowing us to discriminate tetraploid cells with two diploid nuclei (indicating cytokinesis failure) from mononucleated 4c cells (indicating endoreplication) (Carvalho et al., 2011; Toledo et al., 2013). Both BCG and BLP stimulation of MΦ precursors induced a significant, MyD88-dependent increase in nuclear area and in DNA content per single nucleus (Figures 2D–2F). Fluorescence in situ hybridization (FISH) in interphase nuclei confirmed increased DNA content per nucleus (Figures 2G and 2H).

QIBC analysis of the DNA content of single nuclei was combined with IF for β-tubulin to accurately identify single cells and revealed that the majority (74.8%) of polyploid nuclei were contained within BiNucl cells, whereas 16% of polyploid nuclei were contained within MoNucl cells (Figure 2I). These data show that chronic stimulation with BLP promoted recurrent cytokinesis failure and, to a lesser extent, endoreplication (Figures S5D and S5G) leading to the formation of polyploid MMΦ and polyploid MoNucl MΦ, respectively.

In vivo, polyploid nuclei were identifiable in liver granulomas induced by BCG (Figure S5F), albeit in small numbers. Infection

Figure 2. MMΦ Formation from MΦ Precursors Does Not Involve Cell-to-Cell Fusion

(A) IF for CD45.1, CD45.2 in stimulated MΦ precursors. White arrows, CD45.1$^+$CD45.2$^-$ MMΦ (middle), CD45.1$^+$CD45.2$^+$ osteoclast-like MMΦ (bottom).

(B and C) IF for CD45.1, CD45.2 on liver granuloma cryosections from BCG-infected CD45.1:CD45.2 chimeras. (B) Example of a CD45.1$^+$CD45.2$^-$ MMΦ. (C) Numbers of BiNucl and MMΦ with the indicated phenotype; n = 5 chimeras, N.D., not detectable.

(D–K) BLPs and mycobacteria regulate nuclear ploidy (D–F and I): QIBC (G, H, J, and K): FISH. (D) Nuclear area per single nucleus. Black line, mean nuclear area. One representative experiment of three independent experiments. (E and F) DNA content per nucleus. (E) Representative histograms. Red line, cutoff for DNA content >4c. (F) Percentage of polyploid (>4c) nuclei, as in (E). Mean ± SD from three independent experiments. (G and H) FISH for chromosomes 2, 11, X, 16 in vitro. (G) Representative images. (H) Percentage of total nuclei with the indicated number of FISH signals. 155–212 nuclei per condition were analyzed. Mean ± SD from three independent experiments. (I) Distribution of polyploid nuclei in BLP-stimulated MoNucl, BiNucl, and MultiNucl cells. (J and K) FISH for chromosomes 2, 11 in lung cryosections from *M. tuberculosis*-infected WT and *Il13*^{Tg} mice. (J) Representative images. (K) Numbers of polyploid (FISH signals ≥2;2 per nucleus) nuclei from 25 visual fields in MΦ-rich granuloma areas.

*p < 0.05, **p < 0.01, ***p < 0.001; scale bars, 10 μm. See also Figure S5.

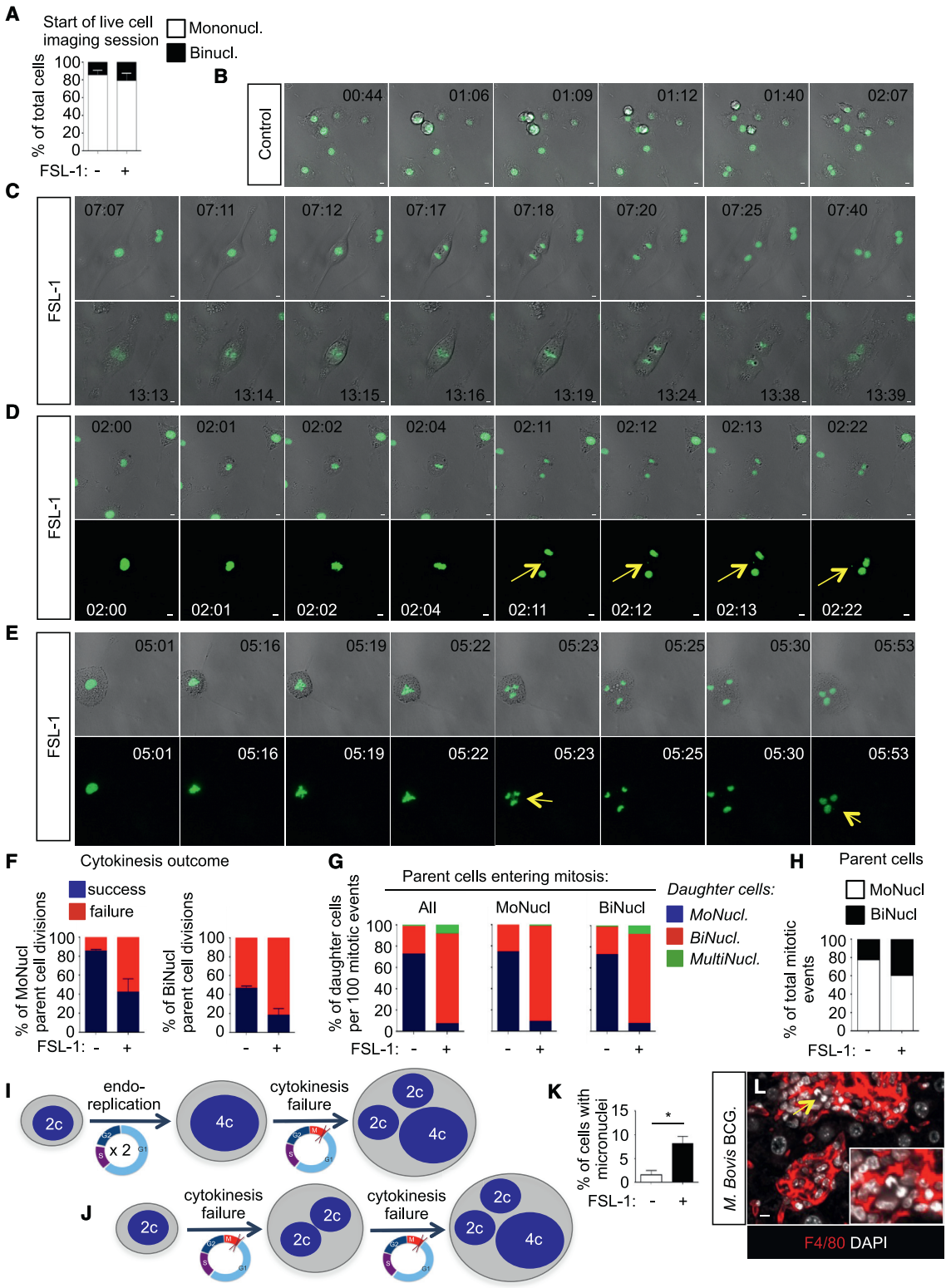

Figure 3. TLR2-Induced MMΦ Formation by Cytokinesis Failure

(A–H) Time-lapse imaging of MΦ precursors after 72 hr of stimulation. (A) Percentage of MoNucl, BiNucl, and MultiNucl MΦ at the beginning of the imaging session. Mean ± SD from three independent experiments.

(legend continued on next page)

of B6 mice with *M. tuberculosis* does not induce the formation of multinucleated giant cells nor granuloma necrosis, both important features of human tuberculosis. In contrast, IL-13-overexpressing ($Il13^{Tg}$) mice form pulmonary necrotizing granulomas with numerous MMΦ, foam cells, and TNF-producing MΦ (Heitmann et al., 2014). Strikingly, the presence of polyploid nuclei was increased in MΦ-rich areas of *M. tuberculosis*-infected $Il13^{Tg}$ lung granulomas as shown by FISH for chromosomes 2 and 11 (Figures 2J and 2K). Collectively, these data demonstrate that *Mycobacteria* and BLP controlled DNA content of MΦ in a process that required signaling via the adaptor protein MyD88.

Continuous Stimulation with BLP Introduces Mitotic Defects Leading to MMΦ Formation

To directly assess whether the formation of MMΦ may occur by modifying cytokinesis, we employed time-lapse live-cell imaging (LCI) of MΦ precursors transduced with a retrovirus encoding the histone protein 2B (H2B) fused with GFP. At the beginning of the LCI session, more than 80% of the cells were MoNucl MΦ (Figure 3A). MoNucl MΦ precursors that were stimulated with M-CSF only were small and underwent predominantly successful divisions (Figure 3B; Movie S1). In contrast, MoNucl cells stimulated with BLP appeared large (Figures 3C–3E) and underwent cytokinesis failure with significantly increased frequency, producing predominantly BiNucl progeny (Figures 3C–3G; Movies S2 and S3). Surprisingly, LCI analysis of all mitotic events revealed that BiNucl cells re-entered mitosis (Figure 3C; Movie S4), and the proportion of BiNucl cells entering mitosis was increased by BLP (Figure 3H). In addition, BLP significantly increased the rate of cytokinesis failure within mitotic events of BiNucl parent cells (Figure 3F).

We examined whether MMΦ formed following failed division of MoNucl versus BiNucl parent cells (Figures 3I–3J). To address this, we fate mapped 307 single mitotic events by determining the number of nuclei in parent and daughter cells in each single mitotic event and the outcome of cytokinesis (success versus failure). MultiNucl cells were generated more often following failed cytokinesis of BiNucl, rather than MoNucl, parent cells (Figure 3G), indicating that at least one round of cytokinesis failure preceded multinucleation. MMΦ formation from MoNucl parent cells also occurred (Figure 3E; Movies S5), but with less frequency (Figure 3G).

How do BLPs cause cytokinesis failure? Cytokinesis failure can result from perturbations in cleavage furrow formation, cleavage furrow stabilization, midbody formation, or abscission (Normand and King, 2010). Tracking single mitotic events by LCI revealed that cytokinesis failed by cleavage furrow regression (Figure 3C; Movie S2). Chromatin persisting in the midzone is an important cause of cleavage furrow regression and cytokinesis failure in cells with lagging chromosomes or acentric chromosome fragments (Davoli and de Lange, 2011). Indeed, lagging chromosomes at the cleavage furrow were present in BLP-stimulated MΦ precursors (Figures 3D and 3E, bottom panels; Movies S6 and S7). Lagging chromosomes or chromatid fragments that fail to be included in the daughter nuclei following cytokinesis failure are eventually enclosed by a nuclear membrane, forming a micronucleus (MN) (Fenech et al., 2011). We quantified MN by QIBC of interphase MΦ. This analysis revealed that BLP induced a significant increase in the numbers of MΦ containing MN (Figure 3K). Importantly, we also identified lagging chromosomes at anaphases of dividing MΦ in BCG-induced granulomas, indicating that such mitotic defects also occurred in granuloma-associated MMΦ in vivo (Figure 3L). Collectively, the data demonstrated that BLP promoted the formation of polyploid MΦ via mitotic defects.

TLR2 Signaling Confers a Proliferation Advantage to Polyploid Macrophage Progeny

We interrogated cell cycle-related gene expression signatures in BLP-stimulated MΦ. BLP stimulation downregulated the expression of cell cycle genes and proteins at the onset of MMΦ formation (day 3), by gene set enrichment analysis (GSEA) (Figure 4A), qRT-PCR, and IB for cyclin D1 and D2 (Figures S6A and S6B). In contrast, following MMΦ formation (day 6), cell-cycle genes were significantly enriched among the genes that were upregulated by BLP (Figure 4A). scRNA-seq at the same time point (day 6) revealed upregulated expression of the mitotic regulators *Ccnb1* and *Cdk1* as well as increased expression of the DNA replication licensing factor *Mcm6* and the DNA synthesis promoting genes *Rrm1* and *Rrm2* in F>4c MΦ (Figure 4B). In addition, gene signatures of DNA replication and cell-cycle progression were highly enriched in FSL1-stimulated MΦ (Figure S4). These data suggested that BLP initially suppressed the proliferation of MΦ precursors (day 3), while at a later time

(B–E) Examples of still images from selected time points. (B) Successful cell divisions in medium without FSL-1. The corresponding movie is Movie S1.
(C–E) Examples of cytokinesis failure outcomes in FSL-1-stimulated MΦ precursors.
(C) Cytokinesis failure leads to a BiNucl daughter cell (top), which re-enters mitosis and re-fails cytokinesis, generating again a BiNucl daughter cell (bottom). The corresponding movies are Movies S2 (top) and S4 (bottom).
(D) Cytokinesis failure leads to a BiNucl daughter cell (top). Lagging chromosome (yellow arrow) visualized at the cleavage furrow, cleavage furrow regression, and formation of a BiNucl daughter cell containing a micronucleus (MN, bottom). The corresponding movies are Movies S3 (top) and S6 (bottom).
(E) MoNucl parent cell undergoes a tripolar mitosis and fails cytokinesis producing a MultiNucl daughter cell (top). Yellow arrows, lagging chromosomes and MN (bottom). The corresponding movies are Movies S5 (top) and S7 (bottom).
(F) Outcome of single-cell divisions from MoNucl and BiNucl parent cells. Mean ± SD from three independent experiments.
(G) Percentage of MoNucl, BiNucl, and MultiNucl daughter cells per 100 mitoses.
(H) Percentage of MoNucl and BiNucl cells entering mitosis during the live-cell imaging session.
(I and J) MMΦ formation via endoreplication and cytokinesis failure (I) or recurrent cytokinesis failure (J).
(K) Percentage of cells containing MN by QIBC. Mean ± SD from three independent experiments.
(L) Lagging chromosomes in a mitotic macrophage in BCG liver granuloma.
(G and H) n > 300 mitotic events, representative of two independent experiments. *$p < 0.05$; scale bars, 10 μm; timescale, hours: minutes. See also Movies S1, S2, S3, S4, S5, S6, and S7.

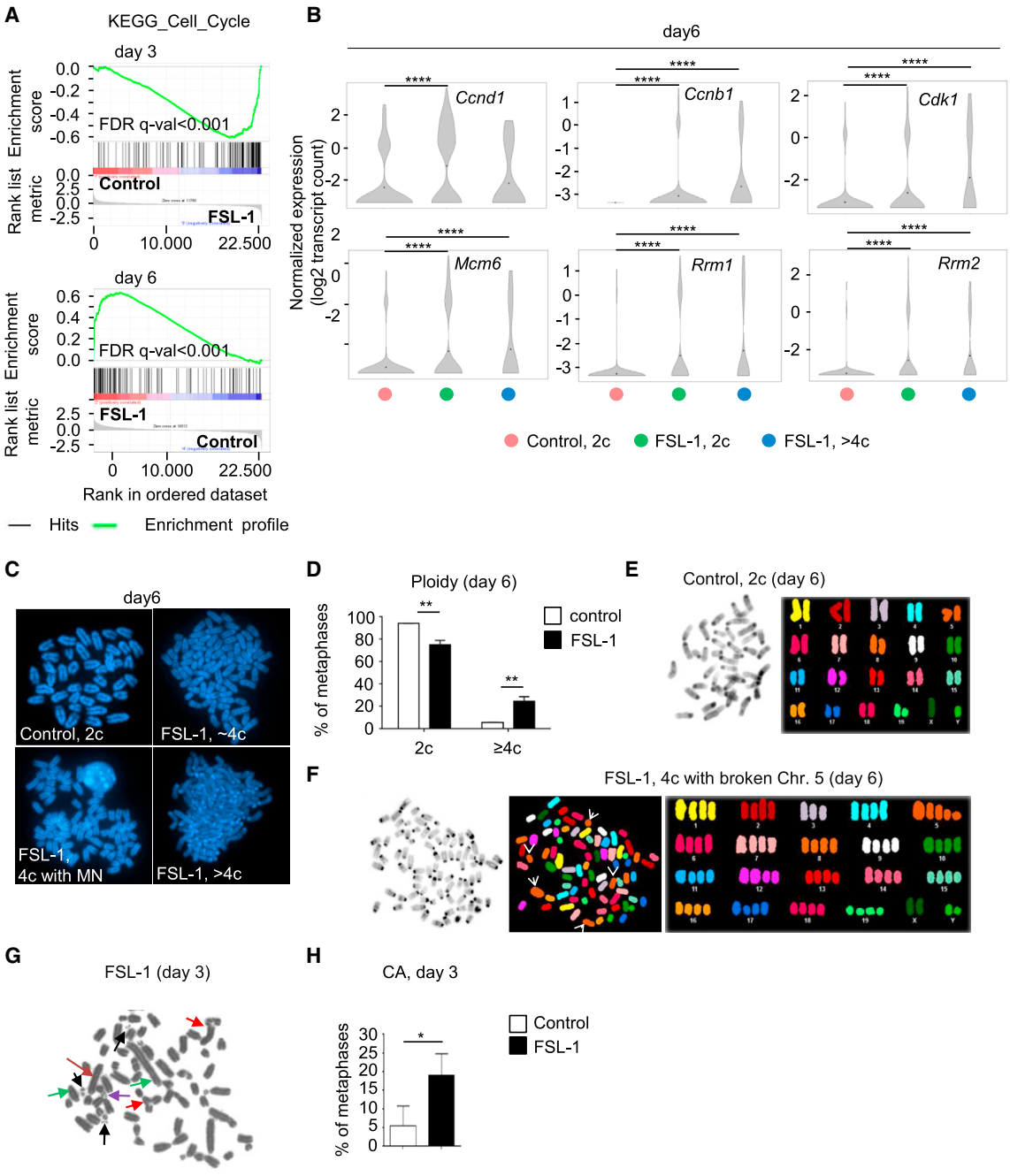

Figure 4. TLR2 Signaling Confers a Proliferation Advantage to Polyploid MΦ Progeny

(A) GSEA for cell-cycle genes. Gene array was performed with four independent biological replicates per group.

(B) Violin plots comparing expression of *Ccnd1, Ccnb1, Cdk1, Mcm6, Rrm1, Rrm2*, by scRNA-seq. y axis, log2 (normalized count+0.1) expression levels; black point, mean of expression level.

(C) Examples of metaphase spreads.

(D) Percentage of metaphases with 2c versus ≥ 4c ploidy. Metaphases with 38–40 chromosomes were grouped as "2c", metaphases with 78–80 or >80 chromosomes were grouped as "≥ 4c". Mean ± SD from three independent experiments. n = 22–101 metaphases per condition.

(E and F) Spectral karyotyping (SKY). Ten metaphases per condition were analyzed. (E) Example of control metaphase with a 2c chromosome count. (F) Example of metaphase with a 4c chromosome count after FSL-1 stimulation.

(G and H) BLPs induce chromosomal aberrations (CA). (G) Example of metaphase spread with CA: triradial chromatid exchange (red arrow), dicentric chromosome (green arrow), acentric fragments (black arrow), Robertsonian translocation (brown arrow), and complex rearrangements (three chromosomes, purple arrow). (H) Percentage of all metaphases with CA. Mean ± SD from five independent experiments.

**p < 0.01, ****p < 0.0001. See also Figure S6.

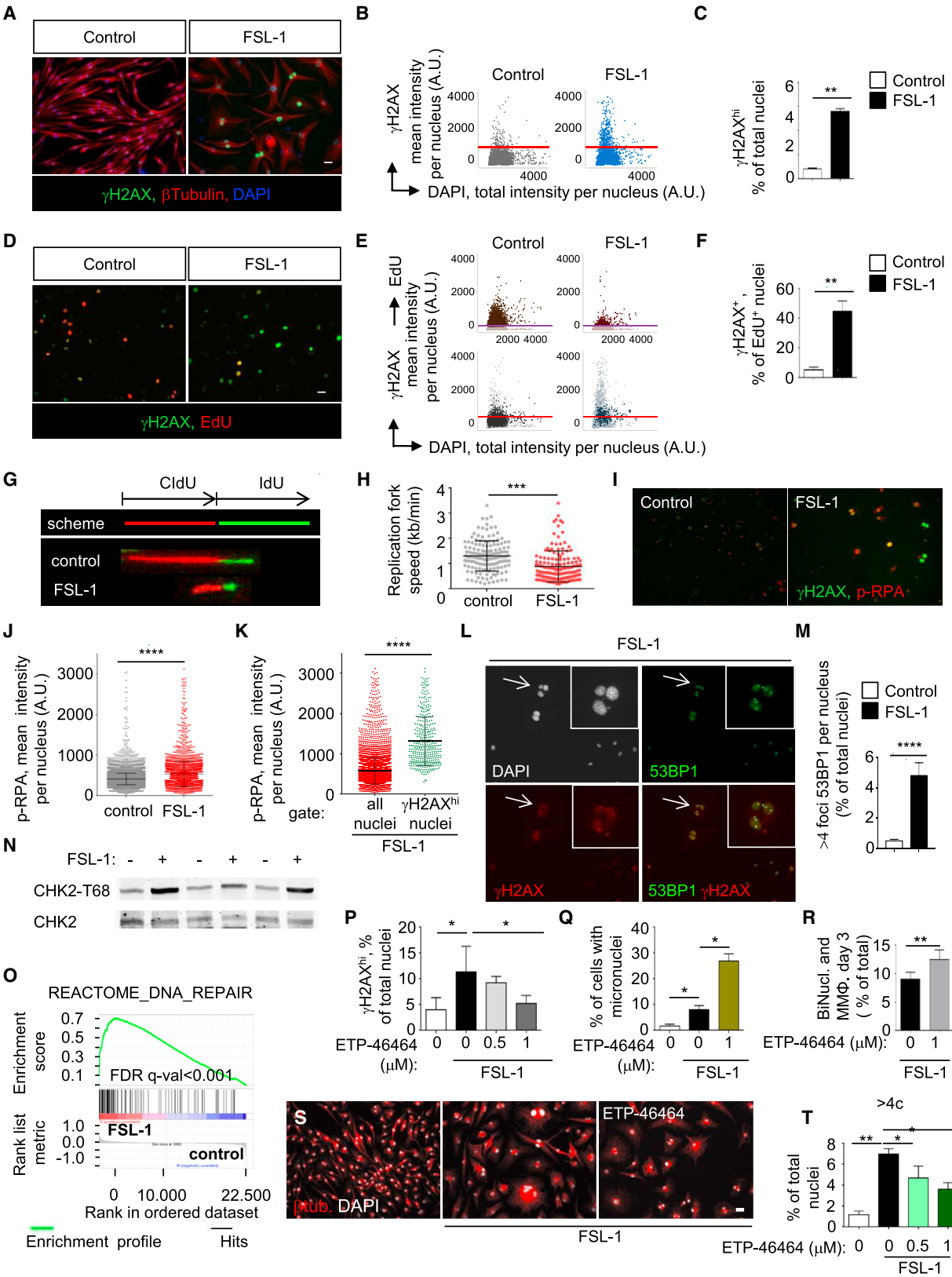

(legend on next page)

point (day 6) BLP re-programmed MMΦ to express cell-cycle genes to promote mitosis and DNA synthesis required for polyploidy.

In agreement, BLP increased the numbers of BiNucl cells entering mitosis (Figure 3H). To confirm that BiNucl cells re-entering mitosis were indeed polyploid and do not represent diploid cells with their DNA divided into subdiploid nuclei, we performed chromosome counts and SKY karyotyping in metaphase spreads. BLP induced a significant increase in polyploid metaphases (Figures 4C–4F), supporting that BLPs promote mitotic entry of polyploid cells. To explore the effects of BLP on DNA synthesis, we quantified bromodeoxyuridine (BrdU) incorporation per single nucleus (Figures S6C–S6E). $BrdU^+$ nuclei with a 2c-4c DNA content (gate A) were gated separately from $BrdU^+$ nuclei with DNA content >4c (gate B; Figure S6D). The rate of BrdU incorporation by nuclei with 2c-4c DNA content was significantly reduced in the presence of BLP in a MyD88-dependent manner (Figure S6E). In contrast, BLP increased the rate of BrdU incorporation into nuclei with DNA content >4c when compared with the few 4c nuclei contained within the control cultures (Figure S6E). Together, these results demonstrate that persistent stimulation with BLP confers a cell-cycle "advantage" to polyploid MΦ, allowing them to bypass proliferation barriers that normally suppress the proliferation of polyploid cells.

Continuous Stimulation with BLP Induces Replication Stress and Activates the DDR

BLP induced a significant increase in micronuclei (Figure 3K) and chromosomal aberrations (Figures 4G and 4H) indicating genomic instability (Fenech et al., 2011), and proliferation of polyploid cells can pose an additional threat to genomic stability (Ganem and Pellman, 2007). Thus, we asked by which pathways BLPs promote the polyploid cell fate via recurrent mitotic defects despite the genomic instability inherent in this process. Replication stress (RS), defined as slowing of DNA synthesis due to stalling of replication fork progression, is intrinsically linked to suppressed DNA synthesis and to activation of the RS response, primarily mediated by the DDR kinase ataxia telangiectasia and Rad3 related (ATR) (Zeman and Cimprich, 2014). To test whether BLP stimulation induced DNA damage signaling in the S phase, we measured the ATR-mediated phosphorylation of the histone variant H2AX (called γH2AX), an early histone modification induced by DNA damage, and correlated its levels with nuclear DNA content by QIBC. MΦ precursors differentiated in the presence of BLP displayed high levels of γH2AX (Figures 5A–5C) often with a pan-nuclear pattern of staining (Figure 5A), consistent with ATR activation and RS (Toledo et al., 2008). γH2AX levels were highest in nuclei with DNA content between 2c and 4c (Figure 5B). EdU^+ nuclei of BLP-stimulated MΦ expressed high levels of γH2AX (Figures 5D–5F), and BLP suppressed the rate of replication fork progression in DNA combing assays (Figures 5G and 5H) and increased levels of phosphorylated (p-)RPA (Replication Protein A), both of which demonstrate RS (Figures 5I and 5J). Importantly, nuclei with high γH2AX levels also had high p-RPA levels (Figure 5K), consistent with an ongoing RS response. RS and activated DDR in BLP-stimulated MΦ was further confirmed by p53-binding protein 1 (53BP1) foci (Lukas et al., 2011) and p-CHK2 (Checkpoint Kinase 2) (Bartek and Lukas, 2003) (Figures 5L–5N). Together, these data demonstrated that BLPs induce RS and activate the DDR in MΦ precursors.

ATR-Dependent DDR Pathways Secure Genomic Stability Further Promoting MΦ Polyploidy

Our data indicated that TLR2 signaling induces RS and activates the DDR initiating DNA repair processes in MΦ as indicated by GSEA analysis showing significant enrichment for cell-cycle repair genes (false discovery rate [FDR] <0.001) (Figure 5O), a finding confirmed by scRNA-seq (Figure S4). We examined the effects of pharmacological inhibition of ATR using low concentrations of a highly specific inhibitor, ETP-46464 (Toledo et al., 2011). ATR inhibition significantly suppressed the levels of γH2AX during MΦ differentiation in the presence of BLP (Figure 5P) and increased mitotic defects and genomic instability as demonstrated by the significantly augmented numbers of MN (Figure 5Q). These data suggest that ATR inhibition increased RS (Toledo et al., 2011). Indeed, BLP-stimulated MΦ showed increased cytokinesis failure after ATR inhibition as evidenced by increased numbers of BiNucl MΦ (Figure 5R). Thus, ATR limits RS while, on the other side, it is known to enhance genomic stability of binucleated cells and may support their re-replication. In agreement, ATR inhibition decreased the DNA content per individual nucleus, indicating decreased re-replication (Figures 5S and 5T). Thus, ATR limits mitotic defects and

Figure 5. BLPs Induce RS and Activate the DDR

(A–F) TLR2-induced DDR in the S phase, QIBC; (A–C) IF for γH2AX, DAPI. (A) Representative images. (B) Mean γH2AX signals per nucleus versus total DAPI intensity. Red lines, cutoff for $\gamma H2AX^{hi}$ nuclei. (C) Percentage of $\gamma H2AX^{hi}$ nuclei, as in (B). (D–F) IF for γH2AX levels, DAPI, and EdU incorporation. (D) Representative images. (E) Mean EdU versus total DAPI intensity (top) and γH2AX versus total DAPI intensity (bottom). Purple line (top), cutoff for EdU positivity. Darker dots bottom, Edu^+ nuclei. Red line (bottom), cutoff for γH2AX positivity. (F) Percentage of EdU^+ nuclei that are $\gamma H2AX^+$, as in (E).

(G and H) Replication fork speed, by DNA combing. (G) Examples of combed DNA fibers with replication tracts: IdU (green), CIdU (red). (H) Replication fork speed distribution. Data are pooled from five independent experiments with n = 250 fibers scored per condition.

(I–K) Regulation of p-RPA levels by BLP, QIBC. (I) Representative images. (J and K) p-RPA levels per single nucleus; J: control versus FSL-1; K: FSL-1 $\gamma H2AX^{hi}$ versus FSL-1 $\gamma H2AX^{lo/hi}$.

(L and M) Regulation of 53BP1 foci by BLP, QIBC. (L) Representative images. (M) Percentage of nuclei with more than four 53BP1 foci per nucleus.

(N) IB for p-ChK2.

(O) GSEA for the REACTOME_DNA_repair gene set. Gene array was performed with four independent biological replicates per group.

(P–T) ATR mediates polyploidy and genetic stability, QIBC. (P) Percentage of $\gamma H2AX^{hi}$ nuclei; cutoff for $\gamma H2AX^{hi}$ expression as in (E). (Q) Percentage of cells with MN. (R) Percentage of BiNucl and MMΦ. (S and T) DNA content per single nucleus. (S) Representative images. (T) Percentage of polyploid (>4c) nuclei.

Mean ± SD from three (C, F, P, Q, R, and T) or two (M) independent experiments are shown. Example from two (J and K) and three (N) independent experiments. *$p < 0.05$, **$p < 0.01$; scale bar, 10 μm.

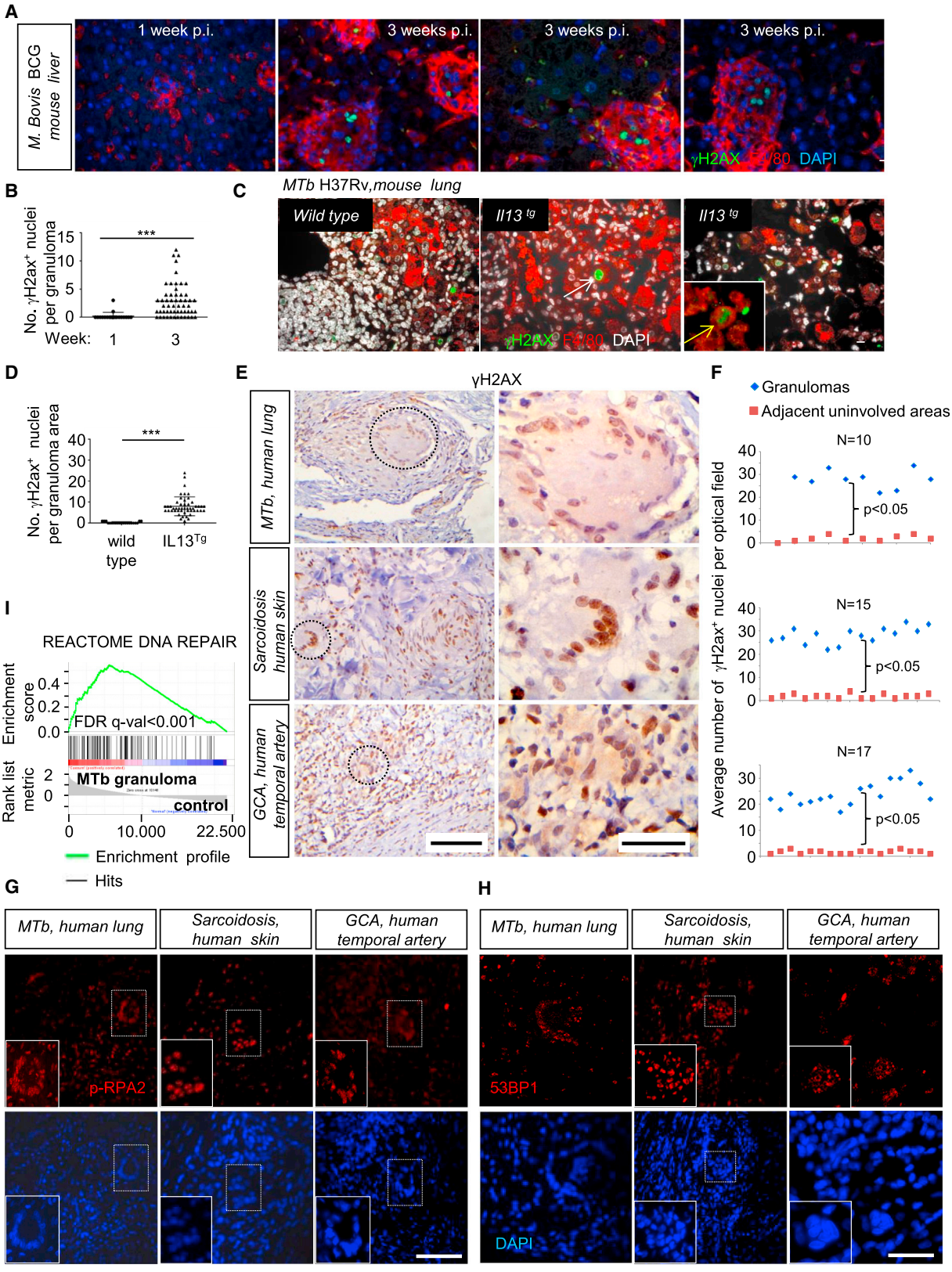

(legend on next page)

genomic instability but, at the same time, is required to support the re-replication of BiNucl MΦ.

RS and Activated DDR in Human and Mouse Granulomas

To test whether MΦ precursor differentiation into polyploid MΦ occurs in the context of RS in vivo, we examined BCG-induced liver granulomas. Strikingly, 3 weeks after infection, γH2AX levels were significantly increased in granuloma-associated MΦ and the increased γH2AX signals co-localized with BiNucl MΦ and MMΦ at the granuloma core (Figures 6A and 6B). Furthermore, γH2AX^{hi} MΦ displayed a pan-nuclear γH2AX staining pattern, consistent with RS (Figure 6A). Similarly, *M. tuberculosis*-induced lung granuloma MΦ of *Il13*^{Tg} mice displayed high levels of γH2AX with a pan-nuclear staining pattern (Figures 6C and 6D) and large F4/80^{+} γH2AX^{hi} mitotic figures, some of them with lagging chromosomes (Figure 6C). The data support that RS and mitotic defects are prominent features under inflammatory conditions in vivo that lead to severe granulomatous immunopathology and promote differentiation of polyploid MΦ.

Next, we analyzed ten human biopsies from *M. tuberculosis*-infected patients. MΦ in granuloma areas containing MMΦ showed significantly increased levels of pan-nuclear γH2AX (Figures 6E, 6F, and S7A). Upregulation of γH2AX was prominent in MMΦ, supporting a role for the DDR pathway in MMΦ differentiation in human *M. tuberculosis* granulomas. To confirm that increased pan-nuclear γH2AX represents RS and activated DDR, we examined p-RPA expression and numbers of 53BP1 foci. Both were prominently increased in MMΦ (Figures 6G, 6H, S7B, and S7C). These findings could be extended to sarcoidosis and giant cell arteritis granulomas (Figures 6E–6H). GSEA analysis of previously published gene expression data (Kim et al., 2010; Subbian et al., 2015) from caseous human lung *M. tuberculosis* granulomas and normal human lung tissue revealed significant enrichment for DNA repair genes (FDR <0.001; Figure 6I). Collectively, the data suggest that RS and activated DDR are crucial determinants of MMΦ differentiation in a larger spectrum of human MMΦ-rich granulomas of infectious and non-infectious etiology.

TLR2-Induced Myc Activation Controls RS and Bypasses p53 Barriers to Proliferation

The proliferation potential of genetically unstable polyploid cells is countered by p53-dependent barriers leading to cell-cycle arrest (Andreassen et al., 2001; Bartkova et al., 2006; Fujiwara et al., 2005; Ganem and Pellman, 2007). GSEA revealed a highly significant enrichment for p53-dependent genes among those upregulated by BLP (Figure S7D). We hypothesized that activated p53 signaling poses a barrier to the differentiation of MΦ precursors into polyploid MΦ and their re-replication, a barrier that is bypassed in the presence of a chronically persisting inflammatory stimulus. To address this, we analyzed numbers of BiNucl MΦ and MMΦ and nuclear ploidy in BM-derived *p53*$^{-/-}$ MΦ and wild-type controls, with and without stimulation with BLP. BLP stimulation of *p53*$^{-/-}$ MΦ precursors generated a strikingly increased number of BiNucl MΦ and MMΦ (Figures 7A and 7B), and nuclear ploidy was significantly upregulated (Figure 7C). These data confirm that p53 poses a barrier to the formation and proliferation of polyploid MΦ by BLP.

We then sought to explain how BLP activated the DDR and licensed the differentiation of polyploid MΦ. An important target of growth factor signaling is the transcription factor Myc, a known inducer of RS as well as a master regulator of cellular proliferation and growth. Microarray, gene, and protein expression data in vitro and in vivo demonstrated that MMΦ formation was linked to increased expression of Myc (Figures 1D, 1M, 7D, and 7E). We asked whether the processes controlling MMΦ generation (i.e., RS and proliferation of polyploid cells against p53-imposed barriers) require Myc signaling. To inhibit Myc in a temporally controlled manner and without interfering with the cell cycle of MΦ progenitors, we used 10058-F4, a widely used and highly specific small molecule inhibitor of Myc (Yin et al., 2003). Myc inhibition abrogated high nuclear γH2AX levels (Figures 7F–7H), in particular in proliferating cells (Figures 7I–7J). In line with a role for Myc as a mediator of TLR2-induced RS signaling, Myc inhibition reversed the TLR2-induced suppression of MΦ precursor proliferation (Figures 7I and 7K). Furthermore, the changes in cholesterol metabolism induced by continuous stimulation of MΦ precursors with BLP were a Myc-dependent event (Figures 7L and 7M). Collectively, our data assign a central role to the TLR2-Myc-DDR signaling axis in the cellular cascades driving differentiation of MΦ precursors into MMΦ.

DISCUSSION

The molecular programs that control MΦ differentiation in the presence of a persistent inflammatory stimulus, although critical

Figure 6. RS and Activated DDR in Granulomas Enriched in MMΦ In Vivo

(A and B) IF for γH2AX, mouse liver cryosections. (A) Pan-nuclear staining pattern of γH2AX. Representative images. Scale bars, 10 μm. (B) Numbers of γH2AX^{hi} MΦ per granuloma. n = 3 mice per time point.

(C and D) IF for γH2AX, mouse lung cryosections. (C) Representative images. White arrow, large γH2AX^{+} nucleus, with pan-nuclear staining pattern. Yellow arrow, large F4/80^{+} mitotic figure with lagging chromosome. Scale bars, 10 μm. (D) Numbers of γH2AX^{hi} F4/80^{+} MΦ per granuloma field from three independent experiments. (A and C) Examples of five independent experiments.

(E–H) RS and DDR in human lung, sarcoid skin, and giant cell arteritis granulomas. IH (E and F) and IF (G and H) in formalin-fixed paraffin-embedded sections. (E) Examples from 10 to 15 patient biopsies per granulomatous disease. Scale bars, left: 200 μm, right: 50 μm. (F) Mean values of the number of γH2AX^{hi} nuclei per visual field in MΦ-rich granuloma areas versus adjacent uninvolved tissue per sample. A total of 500–1,000 cells (10 to 20 high-power fields) were evaluated per sample in granuloma and adjacent unaffected regions, respectively. n = 10–17 patient biopsies per group. (G and H) IF for p-RPA2 and 53BP1. Scale bars, 100 μm.

(I) GSEA for the REACTOME_DNA_repair gene set analysis of previously published gene expression data (Kim et al., 2010; Subbian et al., 2015) from caseous human lung *M. tuberculosis* granulomas and normal human lung tissue.

***p < 0.001. See also Figure S7.

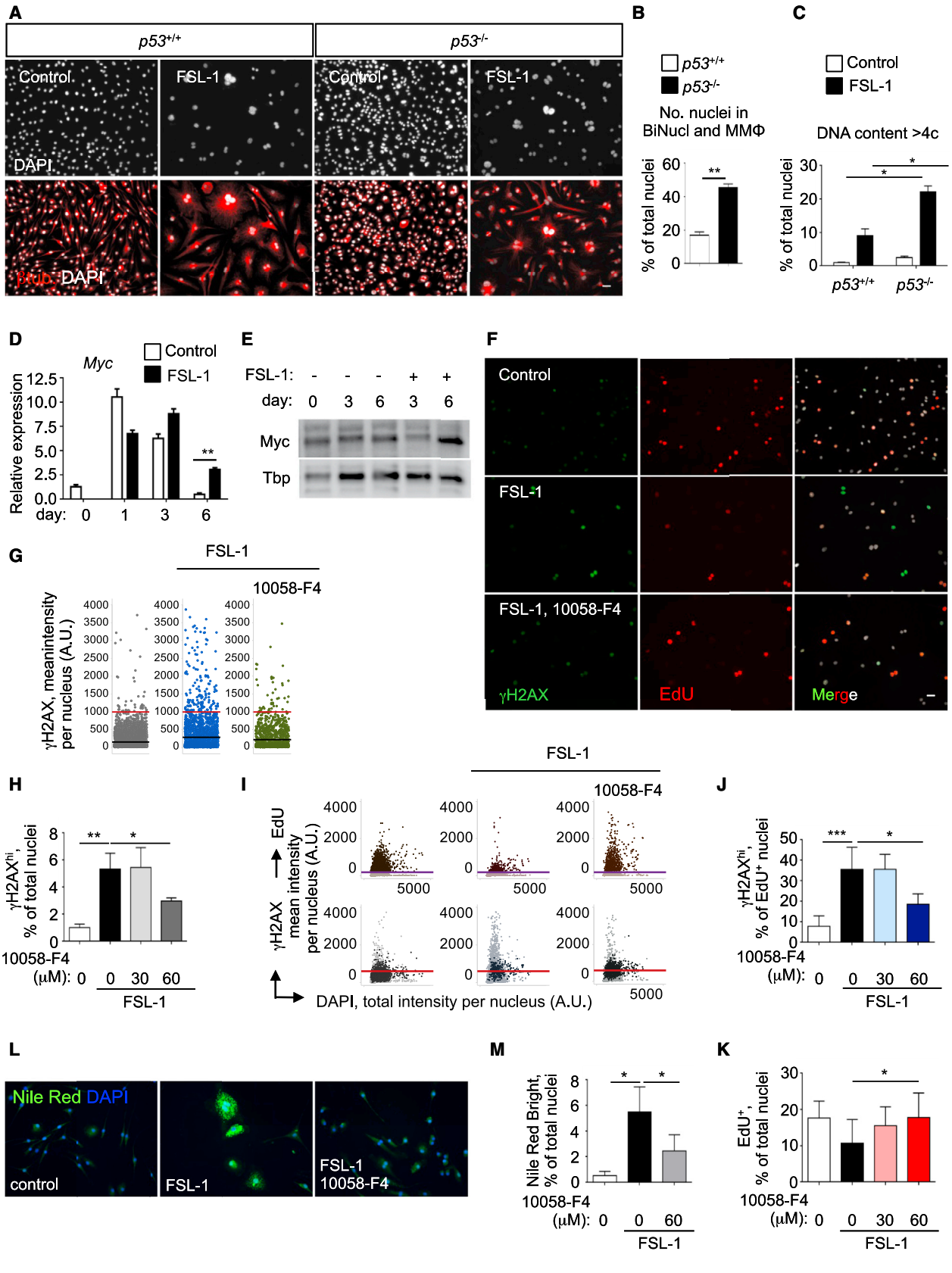

(legend on next page)

for disease outcome, remain unresolved. Here, we delineate a MΦ differentiation pathway induced by chronic stimulation with BLP. Our results unravel a role for Myc-induced DDR signaling as a critical determinant of granuloma-resident polyploid MΦ cell fate with unique metabolic and ECM remodeling gene expression signatures.

Inflammation-Induced Polyploid Macrophage Cell Fate via Modified Cell Divisions

Among immune cells, MΦ are unique in their capability to differentiate into polyploid progeny, such as osteoclasts and MMΦ, in a process widely believed to be cell-to-cell fusion (Helming and Gordon, 2009). How polyploid MΦ subsets arise in the presence of a persistent inflammatory stimulus was, however, unclear. We show that RS and mitotic defects including endoreplication and cytokinesis failure represent an alternative pathway leading to polyploid MΦ subsets in granulomas. Such a pathway to polyploidization was previously described in trophoblasts and hepatocytes (Davoli et al., 2010) but has not been linked to pathogen recognition, inflammatory cytokine signals or immune cell fate. We demonstrate that TLR2 and TNF signaling can engage this pathway in proliferating MΦ precursors leading to the formation of polyploid MΦ.

An intriguing implication of our findings is that distinct cytokine or pathogen-recognition signals may govern the decision to amplify the genomic content of MΦ, producing polyploid progeny by two distinct cellular processes, one being cell-to-cell fusion and the other modified cell division. Thus, RANKL induced cell-to-cell fusion, while TLR2 ligands and TNF led to polyploidization via mitotic defects. Despite the obvious cell biological differences of the "cell-to-cell fusion" and "modified cell division" pathways to polyploidy, our data support that the two pathways share some common mechanistic pillars. Thus, MafB suppression and Myc activation are common regulators of RANKL-induced osteoclastogenesis (Kim et al., 2007; Park-Min et al., 2014) and BLP-induced MMΦ formation.

A TLR2-Myc-DDR Signaling Axis Instructs a Polyploid Macrophage Fate in Granulomas

BLP instructed a non-canonical MΦ differentiation program that led to the formation of polyploid MΦ with an ECM remodeling gene expression signature. Overexpression of the canonical MΦ transcription factor MafB suppressed MMΦ differentiation, denoting their diverging cell fate. The transcription factors MafB and c-Maf were recently shown to repress a MΦ-specific enhancer repertoire associated with self-renewal signaling networks, including Myc as a key signaling node (Soucie et al., 2016).

We identified Myc as a crucial regulator of the BLP-induced DDR response. Interestingly, recent studies reported that the DNA damage pathway was significantly enriched among genes regulated by Myc inhibitors in osteoclast precursors (Park-Min et al., 2014). It is therefore likely that Myc-DDR signaling plays a broad and important role in genomic stability during formation of polyploid MΦ subsets, either by RANKL-induced cell-to-cell fusion or by TLR2 or TNF-induced modified cell division. The mechanisms by which this occurs may differ in the two processes. It will be an important avenue for future research to determine distinct and common mechanisms to protect genomic integrity during MΦ polyploidization as this may provide insights how to promote or suppress MMΦ or osteoclast differentiation thereby modifying disease outcome.

Oncogene-induced RS is a barrier toward tetraploidy and tumorigenesis since the DDR induces cell-cycle arrest and p53-dependent cell death (Bartkova et al., 2006; Gorgoulis et al., 2005). In agreement, TLR2-Myc-mediated RS suppressed cell-cycle progression in diploid MΦ precursors and p53 deficiency significantly increased the numbers of polyploid MMΦ. Strikingly, TNF also acted as a barrier to MMΦ formation since *Tnf*$^{-/-}$ MΦ precursors formed significantly increased numbers of MMΦ. Whether the p53 and TNF-signaling networks cross-talk to suppress MΦ polyploidy is currently unknown. The role of Myc in MΦ polyploidization is in line with recent findings that growth factor signaling may be one route to overcome p53-imposed cell-cycle arrest in tetraploid cells (Ganem et al., 2014). Our findings support that, in non-malignant inflammatory microenvironments, overcoming inflammation-induced p53 barriers to the proliferation of tetraploid cells may be a rate-limiting step for the formation of polyploid MΦ and immune-mediated pathology in chronic granulomatous diseases. Thus, pathways employed by developing cancer cells surprisingly instruct a polyploid MΦ fate in the presence of chronically persisting inflammatory stimuli.

Figure 7. BLPs Activate the DDR and Induce MΦ Polyploidy via Myc

(A–C) p53 suppresses BLP-induced polyploid MΦ, QIBC. (A) Representative images; (B) percentage of BiNucl and MMΦ; (C) percentage of polyploid (>4c) nuclei. (B and C) Mean ± SD from averages of triplicate replicates from two independent experiments.

(D) qRT-PCR of *Myc* mRNA expression, normalized relative to *Gapdh* mRNA expression. Mean ± SD of triplicate determinants pooled from three independent experiments.

(E) IB of nuclear lysates for Myc. Example of two independent experiments.

(F–H) Myc regulates S phase TLR2-DDR signaling, QIBC. (F) Representative images. (G) Mean γH2AX intensity per nucleus. Red lines, cutoff for γH2AX^{hi} expression. Black lines, mean values. (H) Percentage of γH2AX^{hi} nuclei, as in (G).

(I) Mean EdU versus total DAPI intensity (top) and γH2AX versus total DAPI intensity (bottom). Purple line, cutoff for EdU positivity. Darker dots (bottom), EdU^{+} nuclei. Red line (bottom), cutoff for γH2AX positivity.

(J) Percentage of γH2AX^{+} nuclei, among EdU^{+} nuclei, as in (I).

(K) Percentage of EdU^{+} nuclei, as in (I).

(L and M) Myc regulates BLP-induced lipid droplet accumulation. QIBC of cytoplasmic lipid droplet accumulation. (L) Nile Red IF. (M) Percentage of nuclei associated with Nile Red^{+} cytoplasmic droplets.

(H, J, K, and M) Mean ± SD from three independent experiments. *$p < 0.05$, **$p < 0.01$, ***$p < 0.001$, Scale bars, 10 μm.

STAR★METHODS

Detailed methods are provided in the online version of this paper and include the following:

- KEY RESOURCES TABLE
- CONTACT FOR REAGENT AND RESOURCE SHARING
- EXPERIMENTAL MODEL AND SUBJECT DETAILS
  - Human specimens
  - Mice
- METHOD DETAILS
  - Generation of MMΦs from MΦ precursors
  - Bacterial culture and infections
  - Retroviral transductions
  - FISH
  - SKY
  - Immunofluorescence and immunohistochemistry in mouse tissues
  - DNA Fiber Assay
  - Immunohistochemistry (IHC) and Indirect Immunofluorescence (IF) in human samples
  - Time-lapse live-cell imaging
  - Quantitative Image-Based Cytometry (QIBC)
  - qRT-PCR and microarray analysis
  - Single-cell RNA library preparation
  - Quantification of Transcript Abundance
  - Single-Cell RNA Sequencing Data Analysis
  - Laser microdissection and gene expression analysis
  - Immunoblotting
- QUANTIFICATION AND STATISTICAL ANALYSIS
- DATA AVAILABILITY

SUPPLEMENTAL INFORMATION

Supplemental Information includes seven figures, one table, and seven movies and can be found with this article online at http://dx.doi.org/10.1016/j.cell.2016.09.054.

AUTHOR CONTRIBUTIONS

A.T., L.H., and V.H. designed, performed, and analyzed the majority of the experiments with help from K.G., J. Senges, N.M., and T.A. The indicated experiments were performed and analyzed by I.N., T.H. (FISH, SKY, cytogenetics), T.N. (DNA fiber assays, metaphase analysis), S., D.G. (scRNA-seq), K.E., V.G., T.N., R.E.V., and T.G. (human studies), D.E. and M.P. (LCM-MΦ gene expression), S.D.D. (microscopy), and J. Stefanowski, A.E.H., M.M.Z., C.K., and C.D. (osteoclast analysis in vivo). C.H. (*M. tuberculosis* infections), D.P. (microarrays), B.K. (LCI), M.S. (pathology), and M. Follo (QIBC) helped with experiments. D.W., M. Fliegauf, S.S., M.S., and A.J.L.-C. provided critical reagents; L.R. and A.D. analyzed gene array data; S.S., M.H.S., and S.D.D. provided intellectual input. A.J.L.-C. and V.G. provided intellectual input on RS and DDR. V.G. directed the human studies. A.D. co-directed research and revised the manuscript. P.H. oversaw initial experiments. A.T. directed research and wrote the manuscript with input from co-authors.

ACKNOWLEDGMENTS

We thank L. Ivashkiv, Y. Tanriver, M. Lenardo, E. Trompouki, and P. Heun for helpful discussions and R. Rzepka, J. Volz, A. Hölscher, K. Schrenk, M. Vavra, A. Imm, and the Advanced Medical Bioimaging Core Facility of the Charité for excellent technical assistance; C. Blattner and M. Oren for $p53^{-/-}$ mice. The work was supported by the European Union's Seventh Framework Programme (Marie Curie IRG 268390 to A.T. and project INsPiRE to V.G.), the Research Committee of the Medical Faculty, University of Freiburg, an EKFK NAKSYS Fellowship (to A.T.), the DFG (SFB 1160, project 12 to A.T. and R.E.V.; FOR 2165, HA5354/6-1 to A.E.H.; FOR 2033 NicHem, project B1 to C.D.), the German Centre for Infection Research (to C.H.), the BMBF (FKZ01E01502 to S.D.D), the European Research Council (ERC-2012-StG-311377 to A.D. and ERC-2015-StG-679068 to A.J.L.-C.), the Danish Council for Independent Research (Sapere Aude, DFF-Starting Grant 2014 to A.J.L.-C.), the Greek GSRT program of Excellence II (Aristeia II to V.G.). M.H.S. is a BIH-Einstein fellow and INSERM-Helmholtz group leader; he was supported by Agence Nationale de la Recherche' (ANR-11-BSV3-0026), Fondation pour la Recherche Médicale (DEQ. 20110421320), and InCA (13-10/405/AB-LC-HS).

Received: January 21, 2016
Revised: July 26, 2016
Accepted: September 28, 2016
Published: October 27, 2016

REFERENCES

Anders, S., and Huber, W. (2010). Differential expression analysis for sequence count data. Genome Biol. *11*, R106.

Andreassen, P.R., Lohez, O.D., Lacroix, F.B., and Margolis, R.L. (2001). Tetraploid state induces p53-dependent arrest of nontransformed mammalian cells in G1. Mol. Biol. Cell *12*, 1315–1328.

Baker, S.C., Bauer, S.R., Beyer, R.P., Brenton, J.D., Bromley, B., Burrill, J., Causton, H., Conley, M.P., Elespuru, R., Fero, M., et al.; External RNA Controls Consortium (2005). The External RNA Controls Consortium: A progress report. Nat. Methods *2*, 731–734.

Bartek, J., and Lukas, J. (2003). Chk1 and Chk2 kinases in checkpoint control and cancer. Cancer Cell *3*, 421–429.

Bartkova, J., Rezaei, N., Liontos, M., Karakaidos, P., Kletsas, D., Issaeva, N., Vassiliou, L.V., Kolettas, E., Niforou, K., Zoumpourlis, V.C., et al. (2006). Oncogene-induced senescence is part of the tumorigenesis barrier imposed by DNA damage checkpoints. Nature *444*, 633–637.

Berte, N., Piee-Staffa, A., Piecha, N., Wang, M., Borgmann, K., Kaina, B., and Nikolova, T. (2016). Targeting homologous recombination by pharmacological inhibitors enhances the killing response of glioblastoma cells treated with alkylating drugs. Mol. Cancer Ther. Published online July 29, 2016 molcanther.0176.2016.

Carvalho, C.R., Clarindo, W.R., and Abreu, I.S. (2011). Image cytometry: Nuclear and chromosomal DNA quantification. Methods Mol. Biol. *689*, 51–68.

Coschi, C.H., Martens, A.L., Ritchie, K., Francis, S.M., Chakrabarti, S., Berube, N.G., and Dick, F.A. (2010). Mitotic chromosome condensation mediated by the retinoblastoma protein is tumor-suppressive. Genes Dev. *24*, 1351–1363.

Davoli, T., and de Lange, T. (2011). The causes and consequences of polyploidy in normal development and cancer. Annu. Rev. Cell Dev. Biol. *27*, 585–610.

Davoli, T., Denchi, E.L., and de Lange, T. (2010). Persistent telomere damage induces bypass of mitosis and tetraploidy. Cell *141*, 81–93.

Emson, C.L., Bell, S.E., Jones, A., Wisden, W., and McKenzie, A.N. (1998). Interleukin (IL)-4-independent induction of immunoglobulin (Ig)E, and perturbation of T cell development in transgenic mice expressing IL-13. J. Exp. Med. *188*, 399–404.

Fenech, M., Kirsch-Volders, M., Natarajan, A.T., Surralles, J., Crott, J.W., Parry, J., Norppa, H., Eastmond, D.A., Tucker, J.D., and Thomas, P. (2011). Molecular mechanisms of micronucleus, nucleoplasmic bridge and nuclear bud formation in mammalian and human cells. Mutagenesis *26*, 125–132.

Fujiwara, T., Bandi, M., Nitta, M., Ivanova, E.V., Bronson, R.T., and Pellman, D. (2005). Cytokinesis failure generating tetraploids promotes tumorigenesis in p53-null cells. Nature *437*, 1043–1047.

Ganem, N.J., and Pellman, D. (2007). Limiting the proliferation of polyploid cells. Cell *131*, 437–440.

Ganem, N.J., Cornils, H., Chiu, S.Y., O'Rourke, K.P., Arnaud, J., Yimlamai, D., Théry, M., Camargo, F.D., and Pellman, D. (2014). Cytokinesis failure triggers hippo tumor suppressor pathway activation. Cell *158*, 833–848.

Geissmann, F., Manz, M.G., Jung, S., Sieweke, M.H., Merad, M., and Ley, K. (2010). Development of monocytes, macrophages, and dendritic cells. Science *327*, 656–661.

Gorgoulis, V.G., Vassiliou, L.V., Karakaidos, P., Zacharatos, P., Kotsinas, A., Liloglou, T., Venere, M., Ditullio, R.A., Jr., Kastrinakis, N.G., Levy, B., et al. (2005). Activation of the DNA damage checkpoint and genomic instability in human precancerous lesions. Nature *434*, 907–913.

Grün, D., Kester, L., and van Oudenaarden, A. (2014). Validation of noise models for single-cell transcriptomics. Nat. Methods *11*, 637–640.

Grün, D., Muraro, M.J., Boisset, J.C., Wiebrands, K., Lyubimova, A., Dharmadhikari, G., van den Born, M., van Es, J., Jansen, E., Clevers, H., et al. (2016). De novo prediction of stem cell identity using single-cell transcriptome data. Cell Stem Cell *19*, 266–277.

Hashimshony, T., Senderovich, N., Avital, G., Klochendler, A., de Leeuw, Y., Anavy, L., Gennert, D., Li, S., Livak, K.J., Rozenblatt-Rosen, O., et al. (2016). CEL-Seq2: sensitive highly-multiplexed single-cell RNA-Seq. Genome Biol. *17*, 77.

Heitmann, L., Abad Dar, M., Schreiber, T., Erdmann, H., Behrends, J., Mckenzie, A.N., Brombacher, F., Ehlers, S., and Hölscher, C. (2014). The IL-13/IL-4Rα axis is involved in tuberculosis-associated pathology. J. Pathol. *234*, 338–350.

Helming, L., and Gordon, S. (2009). Molecular mediators of macrophage fusion. Trends Cell Biol. *19*, 514–522.

Hölscher, C., Reiling, N., Schaible, U.E., Hölscher, A., Bathmann, C., Korbel, D., Lenz, I., Sonntag, T., Kröger, S., Akira, S., et al. (2008). Containment of aerogenic Mycobacterium tuberculosis infection in mice does not require MyD88 adaptor function for TLR2, -4 and -9. Eur. J. Immunol. *38*, 680–694.

Kim, K., Kim, J.H., Lee, J., Jin, H.M., Kook, H., Kim, K.K., Lee, S.Y., and Kim, N. (2007). MafB negatively regulates RANKL-mediated osteoclast differentiation. Blood *109*, 3253–3259.

Kim, M.J., Wainwright, H.C., Locketz, M., Bekker, L.G., Walther, G.B., Dittrich, C., Visser, A., Wang, W., Hsu, F.F., Wiehart, U., et al. (2010). Caseation of human tuberculosis granulomas correlates with elevated host lipid metabolism. EMBO Mol. Med. *2*, 258–274.

Li, H., and Durbin, R. (2010). Fast and accurate long-read alignment with Burrows-Wheeler transform. Bioinformatics *26*, 589–595.

Lukas, C., Savic, V., Bekker-Jensen, S., Doil, C., Neumann, B., Pedersen, R.S., Grøfte, M., Chan, K.L., Hickson, I.D., Bartek, J., and Lukas, J. (2011). 53BP1 nuclear bodies form around DNA lesions generated by mitotic transmission of chromosomes under replication stress. Nat. Cell Biol. *13*, 243–253.

Meyer, L.R., Zweig, A.S., Hinrichs, A.S., Karolchik, D., Kuhn, R.M., Wong, M., Sloan, C.A., Rosenbloom, K.R., Roe, G., Rhead, B., et al. (2013). The UCSC Genome Browser database: Extensions and updates 2013. Nucleic Acids Res. *41*, D64–D69.

Nathan, C. (2009). Taming tuberculosis: A challenge for science and society. Cell Host Microbe *5*, 220–224.

Normand, G., and King, R.W. (2010). Understanding cytokinesis failure. Adv. Exp. Med. Biol. *676*, 27–55.

Park-Min, K.H., Lim, E., Lee, M.J., Park, S.H., Giannopoulou, E., Yarilina, A., van der Meulen, M., Zhao, B., Smithers, N., Witherington, J., et al. (2014). Inhibition of osteoclastogenesis and inflammatory bone resorption by targeting BET proteins and epigenetic regulation. Nat. Commun. *5*, 5418.

Peyron, P., Vaubourgeix, J., Poquet, Y., Levillain, F., Botanch, C., Bardou, F., Daffé, M., Emile, J.F., Marchou, B., Cardona, P.J., et al. (2008). Foamy macrophages from tuberculous patients' granulomas constitute a nutrient-rich reservoir for M. tuberculosis persistence. PLoS Pathog. *4*, e1000204.

Puissegur, M.P., Lay, G., Gilleron, M., Botella, L., Nigou, J., Marrakchi, H., Mari, B., Duteyrat, J.L., Guerardel, Y., Kremer, L., et al. (2007). Mycobacterial lipomannan induces granuloma macrophage fusion via a TLR2-dependent, ADAM9- and beta1 integrin-mediated pathway. J. Immunol. *178*, 3161–3169.

Ramakrishnan, L. (2012). Revisiting the role of the granuloma in tuberculosis. Nat. Rev. Immunol. *12*, 352–366.

Russell, D.G., Cardona, P.J., Kim, M.J., Allain, S., and Altare, F. (2009). Foamy macrophages and the progression of the human tuberculosis granuloma. Nat. Immunol. *10*, 943–948.

Soucie, E.L., Weng, Z., Geirsdóttir, L., Molawi, K., Maurizio, J., Fenouil, R., Mossadegh-Keller, N., Gimenez, G., VanHille, L., Beniazza, M., et al. (2016). Lineage-specific enhancers activate self-renewal genes in macrophages and embryonic stem cells. Science *351*, aad5510.

Subbian, S., Tsenova, L., Kim, M.J., Wainwright, H.C., Visser, A., Bandyopadhyay, N., Bader, J.S., Karakousis, P.C., Murrmann, G.B., Bekker, L.G., et al. (2015). Lesion-Specific Immune Response in Granulomas of Patients with Pulmonary Tuberculosis: A Pilot Study. PLoS ONE *10*, e0132249.

Taylor, J.L., Hattle, J.M., Dreitz, S.A., Troudt, J.M., Izzo, L.S., Basaraba, R.J., Orme, I.M., Matrisian, L.M., and Izzo, A.A. (2006). Role for matrix metalloproteinase 9 in granuloma formation during pulmonary Mycobacterium tuberculosis infection. Infect. Immun. *74*, 6135–6144.

Toledo, L.I., Murga, M., Gutierrez-Martinez, P., Soria, R., and Fernandez-Capetillo, O. (2008). ATR signaling can drive cells into senescence in the absence of DNA breaks. Genes Dev. *22*, 297–302.

Toledo, L.I., Murga, M., Zur, R., Soria, R., Rodriguez, A., Martinez, S., Oyarzabal, J., Pastor, J., Bischoff, J.R., and Fernandez-Capetillo, O. (2011). A cell-based screen identifies ATR inhibitors with synthetic lethal properties for cancer-associated mutations. Nat. Struct. Mol. Biol. *18*, 721–727.

Toledo, L.I., Altmeyer, M., Rask, M.B., Lukas, C., Larsen, D.H., Povlsen, L.K., Bekker-Jensen, S., Mailand, N., Bartek, J., and Lukas, J. (2013). ATR prohibits replication catastrophe by preventing global exhaustion of RPA. Cell *155*, 1088–1103.

van der Maaten, L., and Hinton, G. (2008). Visualizing data using t-SNE. J. Mach. Learn. Res. *9*, 2579–2605.

Vignery, A. (2005). Macrophage fusion: The making of osteoclasts and giant cells. J. Exp. Med. *202*, 337–340.

Volkman, H.E., Pozos, T.C., Zheng, J., Davis, J.M., Rawls, J.F., and Ramakrishnan, L. (2010). Tuberculous granuloma induction via interaction of a bacterial secreted protein with host epithelium. Science *327*, 466–469.

Williams, G.T., and Williams, W.J. (1983). Granulomatous inflammation–a review. J. Clin. Pathol. *36*, 723–733.

Yin, X., Giap, C., Lazo, J.S., and Prochownik, E.V. (2003). Low molecular weight inhibitors of Myc-Max interaction and function. Oncogene *22*, 6151–6159.

Yu, G., and He, Q.Y. (2016). ReactomePA: An R/Bioconductor package for reactome pathway analysis and visualization. Mol. Biosyst. *12*, 477–479.

Zehentmeier, S., Cseresnyes, Z., Escribano Navarro, J., Niesner, R.A., and Hauser, A.E. (2015). Automated quantification of hematopoietic cell—stromal cell interactions in histological images of undecalcified bone. J. Vis. Exp. (98)

Zeman, M.K., and Cimprich, K.A. (2014). Causes and consequences of replication stress. Nat. Cell Biol. *16*, 2–9.

STAR★METHODS

KEY RESOURCES TABLE

REAGENT or RESOURCE	SOURCE	IDENTIFIER
Antibodies		
IF: anti-CD45.1-PE (clone A20)	eBioscience	Cat# 12-0453
IF: anti-CD45.2-FITC (clone 104)	eBioscience	Cat# 11-0454
IF: anti-CD45 (clone 30-F11)	eBioscience	Cat# 14-0451-82
IF: anti-CD45.1- Alexa Fluor 488 (clone 104)	Biolegend	Cat# BLD-109816
IF: anti-CD45.2-Alexa Fluor 488 (clone A20)	Biolegend	Cat# BLD-110720
IF: anti-F4/80-Alexa Fluor 647 (clone CI:A3-1)	Bio-Rad (AbD Serotec)	Cat# MCA497A647
IF: anti-F4/80 unconjugated (clone CI:A3-1)	Bio-Rad (AbD Serotec)	Cat# MCA497G
IF: anti-MTB (polyclonal)	Bio-Rad (AbD Serotec)	Cat# OBT0947
IF: anti-γH2AX Ser139 (rabbit monoclonal)	Cell Signaling	Cat# 9718
IF: anti-BrdU antibody (mouse, clone B44)	Becton Dickinson	Cat# 374580
IF: anti-BrdU antibody (rat, clone BU/1))	AbD Serotec	Cat# OBT0030G
WB: anti-p38 (polyclonal)	Cell signaling	Cat# 9212
IF: anti-BrdU antibody (clone BU-1)	Thermo Fisher Scientific	Cat# MA3-071
IF: anti-Ki67 (clone SP6)	Thermo Fisher Scientific	Cat# RM-9106
IF: anti-α-tubulin (clone B-5-1-2)	Sigma-Aldrich	Cat# T5168
IF: anti-phospho RPA32 (S4/S8) (polyclonal)	Bethyl laboratories	Cat# A300-245A
IF:anti-53BP1 (polyclonal)	Abcam	Cat# ab21083
IF:anti-RPA2 (clone 9H8)	Abcam	Cat# ab2175
IF:anti-phospho RPA2 [S4/S8] (polyclonal)	Abcam	Cat# ab87277
WB: anti-TATA-binding protein TBP (clone 1TBP18)	Abcam	Cat# ab818
WB: anti-c-Myc (clone 9E10)	Santa Cruz	Cat# sc-47694
WB: anti-Cyclin D1 (clone A12)	Santa Cruz	Cat# sc-8396
WB: anti-cyclin D2 (M-20, polyclonal)	Santa Cruz	Cat# sc-718
WB: anti-MafB (P-20, goat polyclonal)	Santa Cruz	Cat# sc-10022
IF/IHC: anti-γH2AX Ser139 (clone JBW301)	EMD Millipore	Cat# 05-636
IF: Alexa Fluor 568 goat anti-rabbit	Invitrogen	Cat# A-11011
IF: Alexa Fluor 488 goat anti-mouse	Invitrogen	Cat# A-11001
IF: Alexa Fluor 488 goat anti-rabbit	Invitrogen	Cat# A-11034
IF: Alexa Fluor 546 goat anti-mouse	Invitrogen	Cat# A-11030
Chemicals, Peptides, and Recombinant Proteins		
Recombinant murine M-CSF	Peprotech	Cat# 315-02
Recombinant murine TNF	Peprotech	Cat# 315-01A
Recombinant murine sRANK ligand	Peprotech	Cat# 315-11
Recombinant murine IL-1β	Peprotech	Cat# 211-11B
Recombinant murine IFN-γ	Peprotech	Cat# 315-05
FSL-1	Invivogen	Cat# tlrl-fsl
Pam3CSK4	Invivogen	Cat# tlrl-pms
LPS	Invivogen	Cat# tlrl-eklps
poly (I:C)	Invivogen	Cat# tlrl-pic
Nile Red	Sigma-Aldrich	Cat# N3013
RNase A from bovine pancreas	Sigma-Aldrich	Cat# R4642
ETP-46464	Selleckchem	Cat# S8050

(*Continued on next page*)

Continued

REAGENT or RESOURCE	SOURCE	IDENTIFIER
c-Myc Inhibitor 10058-F4	Calbiochem	Cat# 475956
Polybrene (Hexadimethrine Bromide)	Sigma-Aldrich	Cat# H9268
FuGENE6 Transfection Reagent	Roche	Cat# 11 815 091 001
RNaseOUT	Invitrogen	Cat# 10777-019
Superscript II	Invitrogen	Cat# 18064-014
Second Strand Buffer	Invitrogen	Cat# 10812-014
E. coli DNA ligase	Invitrogen	Cat# 18052-019
E. coli RNaseH	Invitrogen	Cat# 18021-071
E. coli DNA polymerase	Invitrogen	Cat# 18010-025
AMPure XP beads	Beckman Coulter	Cat# A63880
RNAClean XP beads	Beckman Coulter	Cat# A63987
Critical Commercial Assays		
Click-iT EdU Alexa Fluor 488 Imaging Kit	Thermo Fisher Scientific	Cat# C10337
Hemacolor Staining Kit	Merck Millipore	Cat# 1.11661.0001
Ultravision Quanto Detection System HRP DAB kit	Thermo Fisher Scientific	Cat# TL-125-QHD
CalPhos Mammalian Transfection Kit	Clontech	Cat# 631312
RNeasy Micro Kit	QIAGEN	Cat# 74004
ARCTURUS PicoPure RNA Isolation Kit	Thermo Fisher Scientific	Cat# KIT0214
ABsolute QPCR Mix, SYBR Green	Thermo Fisher Scientific	Cat# 1159A
TaqMan Gene Expression Master Mix	Thermo Fisher Scientific	Cat# 4369016
TaqMan PreAmp Master Mix	Thermo Fisher Scientific	Cat# 4391128
High-Capacity RNA-to-cDNA Kit	Thermo Fisher Scientific	Cat# 4387406
iScript cDNA Synthesis Kit	Thermo Fisher Scientific	Cat# 1708871
SkyPaint DNA Kit M-10 for Mouse Chromosomes	Applied Spectral Imaging	Cat# FPRPR0030
MEGAscript T7 Transcription Kit	Ambion	Cat# AM1334
Phusion High-Fidelity PCR Master Mix with HF Buffer	NEB	Cat# M0531
ExoSAP-IT For PCR Product Clean-Up	Affymetrix	Cat# 78200
NEBNext Magnesium RNA Fragmentation Module	NEB	Cat# E6150S
Deposited Data		
Raw microarray data	This paper	http://www.ebi.ac.uk/arrayexpress/ Accession Number: E-MTAB-5085
Raw scRNA-seq data	This paper	NCBI GEO Accession Number, GEO: GSE86929
Experimental Models: Organisms/Strains		
Mouse: C57BL/6J	The Jackson Laboratory	Stock No: 000664
Mouse: IL-13-transgenic (^{tg}) mice	Emson et al., 1998	N/A
Mycobacterium tuberculosis H37rv	ATCC	Cat# 27294
Mycobacterium bovis BCG, strain RIVM derived from strain 1173-P2	Medac, Hamburg	Cat# BCG-Medac
Recombinant DNA		
pMX-Mafb-IRES-Egfp	This paper	N/A
pMXs-IRES-Egfp Retroviral expression vector	Cell Biolabs	Cat# RTV-013
pBABE-H2BGFP	Fred Dick Lab Coschi et al., 2010	Addgene plasmid # 26790
FISH probes		
TK (11qE1) / AurKa (2qH3) red/green	Kreatech	Cat# KBI-30501
RAB9B (XqF1) / DSCR (16qC4) red/green	Kreatech	Cat# KBI-30503

(*Continued on next page*)

Continued

REAGENT or RESOURCE	SOURCE	IDENTIFIER
Sequence-Based Reagents		
qPCR Primer: *Gapdh* Forward: TGGAGAAACCTGCCAAGTATG Reverse: GTTGAAGTCGCAGGAGACAAC	This paper	N/A
qPCR Primer: Mafb Forward: AACGGTAGTGTGGAGGAC Reverse: TCACAGAAAGAACTGAGGA	This paper	N/A
qPCR Primer: *Myc* Forward: AATCCTGTACCTCGTCCGAT Reverse: TCTTCTCCACAGACACCACA	This paper	N/A
qPCR Primer: *Ccnd1* Forward: TGCTACCGACAACGCA Reverse: TCAATCTGTTCCTGGCAGGC	This paper	N/A
qPCR Primer: *Ccnd2* Forward: CGTGTGATGCCCTGACTGAG Reverse: GACTTAGATCCGGCGTTATG	This paper	N/A
Taqman Gene Expression assay: *Emr1* (Mm 00802529_m1)	Thermo Fisher Scientific	Cat# 4331182
Taqman Gene Expression assay: *Apoe* (Mm01307193_g1)	Thermo Fisher Scientific	Cat# 4331182
Taqman Gene Expression assay: *Nfkbiz* (Mm00600522_m1)	Thermo Fisher Scientific	Cat# 4331182
Taqman Gene Expression assay: *Ccl5* (Mm01302427_m1)	Thermo Fisher Scientific	Cat# 4331182
Taqman Gene Expression assay: *Chi3l3* (Mm00657889_mH)	Thermo Fisher Scientific	Cat# 4331182
Taqman Gene Expression assay: *Lox* (Mm00495386_m1)	Thermo Fisher Scientific	Cat# 4331182
Taqman Gene Expression assay: *Ctsk* (Mm00484039_m1)	Thermo Fisher Scientific	Cat# 4331182
Taqman Gene Expression assay: *Mmp9* (Mm 00600163_m1)	Thermo Fisher Scientific	Cat# 4331182
Taqman Gene Expression assay: *Pcna* (Mm00448100_g1)	Thermo Fisher Scientific	Cat# 4331182
Taqman Gene Expression assay: *Ccnd2* (Mm00438070_m1)	Thermo Fisher Scientific	Cat# 4331182
Taqman Gene Expression assay: *Mcm6* (Mm00484848_m1)	Thermo Fisher Scientific	Cat# 4331182
Taqman Gene Expression assay: *Blm* (Mm00476150_m1)	Thermo Fisher Scientific	Cat# 4331182
Taqman Gene Expression assay: *Rad50* (Mm00485504_m1)	Thermo Fisher Scientific	Cat# 4331182
Taqman Gene Expression assay: *Rad52* (Mm00448543_m1)	Thermo Fisher Scientific	Cat# 4331182
Taqman Gene Expression assay: *Myc* (Mm00487804_m1)	Thermo Fisher Scientific	Cat# 4331182
randomhexRT primer GCCTTGGCACCCGAGA ATTCCANNNNNN	Custom made, Integrated DNA technologies	N/A
RNA PCR Primers sequences available from Illumina (RP1, RPI1-RPI12)	Custom made, Integrated DNA technologies	N/A
192 polyT primers with unique molecular index and cell barcode, see Table S1	Custom made, Integrated DNA technologies	N/A

(*Continued on next page*)

Continued

REAGENT or RESOURCE	SOURCE	IDENTIFIER
Software and Algorithms		
FISH imaging software FISHView 2.0	Applied Spectral Imaging	http://www.spectral-imaging.com/products-technologies/capture-analysis/fishview
Spectral imaging Software (Vers. 2.6)	Applied Spectral Imaging	http://www.spectral-imaging.com/
TIBCO Spotfire Software	TIBCO Software	http://spotfire.tibco.com/
Scan^R Acquisition Software	Olympus Life Sciences	http://www.olympus-lifescience.com/de/microscopes/inverted/scanr/
Scan^R Analysis Software	Olympus Life Sciences	http://www.olympus-lifescience.com/de/microscopes/inverted/scanr/
GSEA (version 2.0.13)	Broad Institute	http://software.broadinstitute.org/gsea/index.jsp
R version 3.2.4 and RStudio	The R Foundation	https://www.r-project.org/; https://www.rstudio.com/
ReactomePA, R package	Yu and He, 2016	http://bioconductor.org/packages/release/bioc/html/ReactomePA.html
RaceID2 algorithm	Grün et al., 2016	https://github.com/dgrun/StemID
FISH probes		
TK (11qE1) / AurKa (2qH3) red/green	Kreatech	Cat# KBI-30501
RAB9B (XqF1) / DSCR (16qC4) red/green	Kreatech	Cat# KBI-30503

CONTACT FOR REAGENT AND RESOURCE SHARING

Further information and requests for reagents may be directed to, and will be fulfilled by the corresponding author Antigoni Triantafyllopoulou (antigoni.triantafyllopoulou@uniklinik-freiburg.de).

EXPERIMENTAL MODEL AND SUBJECT DETAILS

Human specimens

Formalin-fixed, paraffin-embedded sections from 10 *M. Tuberculosis* lung, 15 sarcoidosis skin and 10 giant cell arteritis temporal artery biopsies, obtained for diagnostic purposes, were analyzed. The demographics of the patients are listed below.

M. Tuberculosis patients (Borstel Cohort): 6 males and 4 females, 18-72 years old at the time of the biopsy.

Skin sarcoidosis patients (Athens Cohort): 2 males and 13 females, 36-75 years old at the time of the biopsy. Giant cell arteritis patients (Athens Cohort): 2 males and 5 females, 51-67 years old at the time of the biopsy.

Giant cell arteritis patients (Freiburg Cohort): 3 males and 7 females, 65-84 years old at the time of the biopsy.

Protocols for experimental use of clinical samples were approved by the Ethics Committees of the Medical School of Athens (sarcoidosis and giant cell arteritis samples), the University of Freiburg (giant cell arteritis samples) and the University of Lübeck (*M. tuberculosis* samples).

Mice

Conventional C57BL/6 mice were purchased from Charles River or Janvier. IL-13-transgenic (^{tg}) mice were previously described (Emson et al., 1998). 8-12-week old, age- and sex- matched mice were used for all in vitro and in vivo experiments. For the generation of bone marrow chimeras C57BL/6 CD45.2$^+$ mice were lethally γ-irradiated (900 rads) from a cesium source and subsequently re-constituted with a mixture of bone marrow cells from C57BL/6 CD45.2$^+$ and C57BL/6 CD45.1$^+$ congenic mice. For the first 4 weeks, mice received antibiotic-containing drinking water. Animals were allowed to reconstitute for 6-12 weeks prior to infection with *M. bovis* BCG. Following reconstitution bone marrow of chimeric mice contained roughly equal numbers of CD45.1$^+$ and CD45.2$^+$ leukocytes. All animal experiments were approved and performed in accordance with the guidelines of the local animal care and use committees of the Regierungspräsidium Freiburg and Kiel.

METHOD DETAILS

Generation of MMΦs from MΦ precursors

Bone marrow (BM) cells were flushed from the femurs of mice and cultured with murine M-CSF (20 ng/ml, Peprotech) on petri dishes in DMEM supplemented with 10% FBS for 4-5 days. The adherent cell population (referred to as 'macrophage precursors') was then

recovered and plated at 2x10^4 cells/ml in OptiMEM medium containing 10% FBS and 50ng/ml M-CSF in triplicate wells on 96-well plates. FSL-1, Pam3CSK4, LPS, poly (I:C) (all from Invivogen) or TNF, IFN-γ, IL-1β (Peprotech) were added for an additional 6 days, unless otherwise indicated. For MMΦ quantification, 96-well plates were stained using the Hemacolor staining kit (Merck) or DAPI and beta-tubulin. MMΦs (defined as cells containing ≥ 3 nuclei) were quantified in triplicate wells. Osteoclastogenesis using RANKL was done from bone marrow (BM) cells using established protocols, as previously described (Park-Min et al., 2014).

Bacterial culture and infections

Mycobacterium tuberculosis strain H37Rv and *Mycobacterium bovis* BCG were expanded to log phase on Middlebrook 7H9 liquid medium supplemented with ADC (Difco), washed, aliquoted in PBS and stored at −80°C until further use. Bacterial stocks were quantified on 7H11 agar supplemented with OADC (Difco). For mycobacterial infections, animals were inoculated *i.p.* with 2 × 10^6 *Mycobacterium bovis* BCG or infected via the aerosol route with a low dose of 100 CFU *M. tuberculosis* H37Rv, as previously described (Hölscher et al., 2008).

Retroviral transductions

Retrovirus packaging was performed by transfecting the retroviral vectors into Phoenix cells using FuGENE6 (Roche) for the pBABE-H2BGFP vector (pBABE-H2BGFP was a gift from Fred Dick (Addgene plasmid # 26790)) and CalPhos transfection reagent (Clontech) for the *pMX-Mafb-IRES-Egfp* and *pMX-IRES-Egfp* empty vectors. Bone marrow cells were infected with the recombinant retroviruses in the presence of 4μg/ml polybrene and M-CSF (20ng/ml) for 24h, after which the media was changed. After 48h adherent cells were collected, GFP$^+$ cells were sorted and re-plated for stimulation.

FISH

Labeled probes from four different mouse chromosomes; 2qH3(Anurka); 11qE1 (Tlk2); 16qC4(Rcan1); XqF1(Rab9b) were hybridized to methanol-acetic acid fixed cells, according to suppliers instruction (Kreatech). After hybridization and washing cells with specific hybridization signals were photographed using specific sets of filters using fluorescence microscope (Axio Imager, Zeiss) equipped with a CCD camera and digitized images of the FITC, CY3, and DAPI signals of same cell were merged using the FISH imaging software, FISHView 2.0 (Applied Spectral Imaging).

SKY

Metaphase chromosomes were prepared according to standard procedures. Hybridization with mouse SKY chromosome paints (SkYPaint, Applied Spectral Imaging) was carried out following manufacturer's instructions. After hybridization and washing, spectral images were acquired using a HiSky system (SD300) and dedicated Spectral imaging Software (Vers. 2.6). Obtained SKY images were then analyzed by the SkyView software, version 6.0 (Applied Spectral Imaging). Karyotypes depicted in the figures are prepared from the spectrally classified pseudo-colored chromosomes.

Immunofluorescence and immunohistochemistry in mouse tissues

For immunohistochemistry, liver was fixed in 10% formalin, embedded in paraffin and cut into 3–5 μm sections. Paraffin sections were rehydrated and heat-induced antigen retrieval was performed in citrate buffer or TRIS buffer. Immunofluorescence of mixed chimeric livers was performed on 5 μm-thick cryosections, fixed with 4% PFA at room temperature and treated with 0.5% Triton X-100 in PBS for 10 min. Undecalcified bone cryosections were prepared as previously described (Zehentmeier et al., 2015).

For immunofluorescence of in vitro samples, macrophage precursors were plated in 96-well plates (tissue culture-treated, BD falcon black plates) at 2x10^4 cells/ml in OptiMEM (GIBCO) medium with 10% FBS, 50ng/ml M-CSF and stimulated with TLR ligands, cytokines or vehicle. At the indicated time points, the cells were fixed with 4% paraformaldehyde at room temperature for 15 min and treated 0.5% Triton X-100 in PBS for 10 min.

Subsequent to fixation and antigen retrieval or permeabilization, sections or cells were blocked with a solution containing 1% BSA/10% goat serum/0.3% Triton X-100 in PBS and incubated overnight at 4°C with the following primary antibodies, diluted in 1% BSA/0.3% Triton X-100 in PBS: anti-CD45.1-PE (Ebioscience), anti-CD45.2-FITC (Ebioscience), anti-F4/80-Alexa647 or anti-F4/80 unconjugated (AbD Serotec), anti-γH2AX Ser139 (Cell Signaling), anti-Ki67 (Pierce Thermo Scientific), anti-β-tubulin (Sigma), anti-MTB (Serotec). Next, sections or cells were incubated with highly cross-adsorbed secondary antibodies raised against mouse, rabbit or rat and labeled with Alexa 488, Alexa 546 or Alexa 633 Fluorophores (Molecular Probes, Life Technologies), for 1 hr at room temperature. Nuclei were stained with 4',6-Diamidino-2-Phenylindole Dihydrochloride (DAPI, 10 μg/ml in PBS). When Click-it EdU reactions (Molecular Probes, Life Technologies) were combined with antibody staining, these were performed prior to incubation with the primary antibodies, while EdU was added to the medium prior to fixation, following the manufacturer's protocol. For BrdU staining and DNA content analysis, BrdU was added to the medium prior to fixation and incubated for 30 min. Cells were fixed with ice-cold methanol for 10 min at −20°C. Cells were slowly rehydrated with ice-cold PBS, treated with 2N HCl for 1 hr at room temperature to denature DNA, blocked and incubated overnight at 4°C with mouse monoclonal anti-BrdU antibody (Pierce), followed by incubation with secondary antibody as above. Nuclear RNA was digested with DNase free RNase A (Sigma) for 30 min at 37°C and stained with Propidium Iodide (PI) 50 μg/ml for 30 min at room temperature. Alternatively, staining of nuclear DNA with DAPI, following initial fixation with 4% PFA and permeabilization in 0, 5% Triton X-100 in PBS, was equivalent to PI staining for quantitation of nuclear DNA

content by image cytometry. For lipid body staining, cells were fixed for 15 min in PBS-PFA 4%, permeabilized with Triton X 0.1% for 10 min, stained with Nile Red (Sigma-Aldrich, 1:10,000 dilution, from a stock solution of 5mg/ml in acetone) for 5 min, then washed with PBS. Image acquisition of multiple random fields was automated on a ScanR screening station (Olympus, Germany) and analyzed by using ScanR (Olympus, Germany) analysis software.

Bone cryosections were permeabilized using 0.3% Triton X-100 in PBS for 10 min and blocked with 10% goat serum, 1% BSA in PBS for 15 min. Primary antibodies against CD45.1 (BioLegend, Clone 104, BLD-109816), CD45.2 (BioLegend, Clone A20, BLD-110720), CD45 (eBioscience, Clone 30-F11, 14-0451-82) were diluted 1:100 in 1% BSA in PBS staining buffer and incubated for 1-1.5 hr at RT. Secondary antibodies anti-rat Alexa647 (Invitrogen, A-21208) were diluted 1:500 in staining buffer and incubated for 1 hr at RT. Brightfield images were acquired on a Keyence Z-9000 system. Confocal fluorescent and DIC images were acquired with a Nikon A1Rsi+ system using 405 nm, 488 nm and 640 nm laser excitation.

DNA Fiber Assay

DNA fiber assay was performed as described (Berte et al., 2016) with slight modifications. Following stimulation cells were pulse labeled with 25 μM 5-chloro-2′-deoxyuridine (CldU; Sigma) followed by labeling with 250 μM 5-iodo-2′-deoxyuridine (IdU; TCI Deutschland, Eschborn, Germany) for 20 min each. Labeled cells were harvested by scraping in ice-cold PBS and lysed onto SuperFrost slides. DNA fibers were allowed to stretch and were fixed. HCl (2.5 M)-treated fiber spreads were stained with monoclonal rat anti-BrdU (AbD Serotec, 1:1000) followed by monoclonal mouse anti-BrdU (Becton–Dickinson, 1:1500). Primary antibodies were detected by donkey Fab2 anti-rat Cy3-coupled and anti-mouse Alexa488-coupled secondary antibodies (Jackson ImmunoResearch, Europe, 1:500). Fibers were examined and images captured using LSM 710 supplied with ZEN 2009 software (Carl Zeiss, Germany). CldU-labeled and IdU-labeled tracks were measured using LSM Image Browser (Carl Zeiss, Germany) and μm values were converted into kilo base pairs. At least 150 forks were analyzed from 3 repetitions. DNA fiber structures from 3 independent experiments were counted in ImageJ software (Version 1.44p) using the Cell Counter function.

Immunohistochemistry (IHC) and Indirect Immunofluorescence (IF) in human samples

Paraffin sections (4 μm thick) were deparaffinized and gradually rehydrated. Antigen retrieval was carried out in 10mM citrate buffer (pH 6.0) by heating the slides for 25 min in a microwave oven. For IHC the anti-γH2AX primary antibody (05-636, EMD Millipore) diluted 1:1000 in TBS, was applied overnight at 4°C. Blocking and signal detection was carried out with the Ultravision Quanto Detection System HRP DAB kit (Cat no: TL-125-QHD Thermo Scientific) according to manufacturer's instructions. Hematoxylin was used as counterstain. Stainings were observed with the Leica DM 1750M microscope equipped with a DFC 329 Leica digital camera and image acquisition was performed with the Leica Application Suite (LAS) v4.4.0 software. A total of 500-1000 cells (10-20 high power fields) were evaluated in granuloma and adjacent unaffected regions), respectively (when this was feasible due to limited tissue). The mean number of gH2AX positive cells, in these areas (granuloma-adjacent), for each sample per disease was estimated and depicted in histograms. Intra-observer variability was minimal ($p < 0.01$). Statistical tests were performed by the SPSS v17.0.

For IF the following primary antibodies were applied at 4°C overnight: i) anti-53BP1 (ab21083, Abcam), diluted 1:200 in TBS ii) anti-RPA2 (ab2187 [9H8], Abcam), diluted 1:200 in TBS and iii) anti-phospho RPA2 [S4/S8] (ab87277, Abcam), diluted 1:200 in TBS. Slides were treated with blocking solution containing 1% BSA and 5% normal goat serum (Invitrogen, #31873). Secondary antibodies were Alexa Fluor 488 goat anti-mouse IgG (H+L), (Invitrogen, # A-11001), dilution 1:500 in TBS and Alexa Fluor 568 goat anti-rabbit IgG (H+L), (Invitrogen, #A-11011, dilution 1:500 in TBS. Sections were counterstained with 100 ng/ml of 4,6-diamidino-2-phenylindole (DAPI). Image acquisition of multiple random fields was automated on a ScanR screening station (Olympus, Germany) and analyzed by using ScanR (Olympus, Germany) analysis software, or a Zeiss Axiolab fluorescence microscope equipped with a Zeiss Axiocam MRm camera and Achroplan objectives while image acquisition was performed with AxioVision software release 4.7.1.

Samples either previously characterized (for γH2AX and 53BP1 immunoreactivity) or instructed by the manufacturer (for RPA2 and phospho RPA2), served as positive controls while omission of the primary antibody was performed in negative control assays.

Time-lapse live-cell imaging

Live-cell imaging was started at day 3 after stimulation of bone marrow-derived macrophage precursors with FSL-1 (20ng/ml, Invivogen) or medium. Cells were grown in cell culture dishes (Cellbind, Corning) in Optimem (GIBCO) containing 10% FBS and 50ng/ml M-CSF. In some experiments bone marrow macrophage precursors were transduced with retrovirus expressing H2BGFP prior to stimulation, as described above. Similar rates of cytokinesis failure were observed with or without retroviral transduction. Time-lapse live-cell imaging was performed using an LSM 710 confocal microscope equipped with epifluorescence live-cell imaging setup providing a humidified atmosphere at 37°C with 5% CO_2 (Carl Zeiss). Sample illumination was kept to a minimum and had no adverse effects on cell division and proliferation. Differential interference contrast (DIC) and fluorescent (GFP filter) images were acquired every 1-15 min with a 40x Objective. Image analysis was performed using Zeiss ZEN software.

Quantitative Image-Based Cytometry (QIBC)

Image acquisition was performed on an Olympus IX-81 inverse microscope using a UPLSAPO 20x objective (N.A. 0.75) and ScanR Acquisition software, as recently described in detail (Toledo et al., 2013). Acquisition times for the different channels were adjusted to obtain images under non-saturating conditions for all the treatments analyzed within the experiment. For QIBC analysis of single

nuclei in vitro, 25 to 96 images were acquired per well using triplicate wells per condition, containing in total 5000 to 10000 cells per condition. After acquisition, images were processed for automated analysis using the ScanR Analysis software. A dynamic background correction was first applied to the images. DAPI or PI signal was used to generate a mask that identified each individual nucleus as an individual object. This mask was then applied to quantify pixel intensities in the different channels for each individual cell/object. The watershed segmentation algorithm included in the software was applied to separate nuclear clusters. Geometrical parameters (area, circularity, and physical position in the field of view) are calculated for each individual object. After segmentation and pixel quantification, the desired quantified values for each nucleus (mean and total intensities, area) were extracted and data were analyzed using the ScanR and Spotfire softwares to quantify percentages and average values and to generate color-coded scatter diagrams in a flow-cytometry-like fashion. Fragmented and apoptotic nuclei were excluded based on their total DAPI fluorescence, circularity, and nuclear area. Single cell analysis by high content microscopy not only provides the spatial resolution of fluorescence imaging, but also greatly exceeds flow-cytometry and immunoblotting in resolution and quantitative power (Toledo et al., 2013). Particularly given the strong adherence of TLR2-induced polyploid macrophages to their matrix (L.H. and A.T., unpublished data), QIBC was superior in quality and resolution to any technique that required detaching MMΦ, such as collection of cells for flow cytometry, or western blot. Furthermore, QIBC offered the unique advantage of permitting discrimination between multinucleated polyploid macrophages with diploid nuclei from mononucleated polyploid macrophages. Moreover, QIBC allowed us to relate DNA synthesis and DDR to single nuclei for thousands of cells with varying numbers of nuclei and nuclear DNA content, using cell-cycle asynchronous populations.

For QIBC analysis of micronuclei, micronuclei were identified based on total DAPI fluorescence, circularity, and area. For QIBC analysis of nuclear area in granuloma-associated macrophage nuclei, we established the following algorithm: using surface F4/80 expression as a primary object, we gated in granulomas, defined as F4/80$^+$ objects with a large area. A 'large' area of F4/80$^+$ objects was defined based on the presence of more than 20 F4/80$^+$ cells within that area. Within the granuloma gate, single nuclei were identified as secondary objects, based on total DAPI fluorescence, while fragmented nuclei were excluded based on their total DAPI fluorescence and nuclear area. The nuclear area was then analyzed within single granuloma nuclei (Figure 1E). For QIBC analysis of Ki67 expression in F4/80$^+$ cells, all F4/80$^+$ cells were included in the analysis using F4/80 positivity to define the primary object while single nuclei associated with F4/80$^+$ objects were identified as secondary objects, based on their total DAPI fluorescence, excluding fragmented nuclei as above. Ki67 expression within single nuclei was then analyzed (Figure 1H), as percent of total nuclei associated with F4/80$^+$ cells.

For QIBC analysis of lipid bodies, in order to distinguish the lipids contained within lipid bodies from those of the cell membranes, we took advantage of the fluorescent emission spectrum properties of Nile Red, which depend upon the lipid Nile Red is associated with, i.e., for triacylglycerol: λmax em = 590nm, for phospholipids: λ_{max} em = 640nm (Molecular Probes handbook), as previously described (Peyron et al., 2008). On high content images and using the Olympus ScanR analysis software, the phospholipid backgrounds of both lipid and non-lipid body laden macrophages were summed together into joint sub-objects and are displayed in red, while the triacylglycerol-rich lipid bodies appear in white. The threshold for Nile Red positivity was set based on the total Nile Red fluorescence intensity of cells with more than 50% of their cytoplasm stained.

qRT-PCR and microarray analysis

Total RNA was isolated using the RNeasy Micro Kit (QIAGEN) and reversed transcribed using the First Strand cDNA Synthesis kit (Fermentas). qRT-PCR was performed in triplicate using an Eppendorf Realplex Thermal Cycler (Eppendorf), following the manufacturer's protocols. Relative amounts of mRNA were calculated by the ΔΔCt method and normalized for levels of *Gapdh*. The following primer sequences were used: *Myc*, forward 5′-AATCCTGTACCTCGTCCGAT-3′, reverse 5′- TCTTCTCCACAGACACCACA-3′; *Ccnd1*, forward 5′-TGCTACCGACAACGCA-3′, reverse 5′- TCAATCTGTTCCTGGCAGGC-3′; *Ccnd2*, forward 5′-CGTGTGATGC CCTGACTGAG-3′, reverse 5′-GACTTAGATCCGGCGTTATG-3′; *Gapdh*, forward 5′- TGGAGAAACCTGCCAAGTATG −3′, reverse 5′- GTTGAAGTCGCAGGAGACAAC −3′; *Mafb*, forward 5′- AACGGTAGTGTGGAGGAC −3′, reverse 5′- TCACAGAAAGAACTG AGGA −3′. For microarrays, total RNA was isolated using the RNeasy Micro Kit (QIAGEN) and samples with an RIN greater than 8 were further processed with the Ambion WT Expression kit (Ambion, USA) as described by the manufacturer. The resulting cDNAs were fragmented and then labeled using the Affymetrix Terminal Labeling kit (Affymetrix, USA). Labeled fragments were hybridized to Affymetrix GeneChip ST 2.0 arrays for 16 hr at 45°C with 60 rpm in an Affymetrix Hybridization oven 645. After washing and staining, the arrays were scanned with the Affymetrix GeneChip Scanner 3000 7G. CEL files were produced from the raw data with Affymetrix GeneChip Command Console Software Version 3.0.1. For the GSEA analysis (version 2.0.13) differentially expressed genes in each group were compared to the indicated gene sets available on the GSEA homepage. A list of gene sets is available as electronic file. For the heatmap, a selection of genes based on the differences in gene expression, the involvement in immunological processes and the GSEA analysis were plotted.

Single-cell RNA library preparation

Single cell RNA sequencing was performed using CEL-Seq2 method (Hashimshony et al., 2016) with several modifications. A 5-fold volume reduction was achieved using a nanoliter-scale pipetting robot (Mosquito HTS, TTP Labtech). Single cells were sorted into 384-well plates containing 240nL of primer mix (CEL-Seq Primer sequences are listed in Table S1) and 1.2 μL of PCR encapsulation barrier, Vapor-Lock (QIAGEN). Sorted plates were centrifuged at 2200 g for 10min at 4°C, snap-frozen in liquid nitrogen and stored at −80°C until processed. 160nL of reverse transcription reaction mix and 2.2 μL of second strand reaction mix was used to convert

RNA into cDNA. cDNA from 96-cells were pooled together before clean up and in vitro transcription, generating 4 libraries from one 384-well plate. 0.8 μL of AMPure/RNAClean XP beads (Beckman Coulter) per 1 μL of sample were used during all the purification steps including the library cleanup. Other steps were performed as described in the original protocol. Twelve libraries (1152 single cells) were sequenced on a single lane (pair-end multiplexing run, 100bp read length) of an Ilumina HiSeq 2500 sequencing system generating 200 million sequence fragments.

Quantification of Transcript Abundance

Paired end reads were aligned to the transcriptome using bwa (version 0.6.2-r126) with default parameters (Li and Durbin, 2010). The transcriptome contained all RefSeq gene models based on the mouse genome release mm10 downloaded from the UCSC genome browser comprising 31,201 isoforms derived from 23,538 gene loci (Meyer et al., 2013). All isoforms of the same gene were merged to a single gene locus. The 65bp right mate of each read pair was mapped to the ensemble of all gene loci and to the set of 92 ERCC spike-ins in sense direction (Baker et al., 2005). Reads mapping to multiple loci were discarded. The 25bp left read contains the barcode information: the first six bases corresponded to the cell specific barcode followed by six bases representing the unique molecular identifier (UMI). The remainder of the left read contains a polyT stretch. The left read was not used for quantification. For each cell barcode, the number of UMIs per transcript was counted and aggregated across all transcripts derived from the same gene locus. Based on binomial statistics, the number of observed UMIs was converted into transcript counts (Grün et al., 2014).

Single-Cell RNA Sequencing Data Analysis

Twelve libraries (1152 single cells) were sequenced and, after quality controls, data from 563 cells (199 of Ctrl; 333 of F2c and 31 from F > 4c) were further analyzed. We quantified 12,821 genes and down-sampling to 3,000 transcripts per cell was used for data normalization. Identification and visualization of different subpopulations were performed with the RaceID2 algorithm (Grün et al., 2016). Briefly, down-sampling to 3,000 transcripts was used for data normalization. Initial clustering and subsequent outlier cell identification were performed using k-medoids clustering followed by outlier identification. The t-distributed stochastic neighbor embedding (t-SNE) algorithm was used for dimensional reduction and cell cluster visualization (van der Maaten and Hinton, 2008). For better visualization, the t-SNE algorithm is initialized with positions in the embedded space as determined by classical multidimensional scaling. Differentially expressed genes between two subgroups of cells were identified similar to a previously published method (Anders and Huber, 2010). First, negative binomial distributions reflecting the gene expression variability within each subgroup were inferred based on the background model for the expected transcript count variability computed by RaceID2 (Grün et al., 2016). Using these distributions, a p value for the observed difference in transcript counts between the two subgroups was calculated and multiple testing corrected by the Benjamini-Hochberg method. Pathway enrichment analysis was performed on genes exhibiting a minimum of 2-fold expression difference between the two subgroups with a p-adjusted value less than 0.05. Pathway enrichment analysis was performed using R package, ReactomePA based on Reactome pathway database (Yu and He, 2016).

Laser microdissection and gene expression analysis

Microdissection of F4/80^{hi} macrophages and F4/80^{low} binucleated and MMΦ from M. bovis BCG liver granulomas was performed 3 weeks post infection using a Zeiss PALM MicroBeam (Zeiss) instrument. Liver tissue and Kupffer cells were isolated from PBS-treated age- and sex-matched control mice. Fast immunochemistry of serial sections was performed with F4/80 antibody (Serotec). Immunostained sections were counterstained with DAPI to facilitate the identification of mononucleated and multinucleated macrophages. RNA was isolated with the ARCTURUS PicoPure RNA Isolation Kit (Thermo Fisher) and reverse transcription, pre-amplification and real-time PCR were performed using Thermo Fisher reagents according to the manufacturer's recommendations. For gene expression analysis, we used the following TaqMan Gene Expression Assays:

Gapdh (Mm03302249_g1),
Emr1 (Mm 00802529_m1),
Apoe (Mm01307193_g1),
Nfkbiz (Mm00600522_m1),
Ccl5 (Mm01302427_m1),
Chi3l3 (Mm00657889_mH),
Lox (Mm00495386_m1),
Ctsk (Mm00484039_m1),
Mmp9 (Mm 00600163_m1),
Pcna (Mm00448100_g1),
Ccnd2 (Mm00438070_m1),
Mcm6 (Mm00484848_m1),
Blm (Mm00476150_m1),
Rad50 (Mm00485504_m1),
Rad52 (Mm00448543_m1) and
Myc(Mm00487804_m1).

Immunoblotting

Whole cell extracts and nuclear extracts were obtained and stored at −80C° until processing for Immunoblot. Lysates of equal cell numbers were fractionated on 12% polyacrylamide gels by SDS-PAGE, transferred to polyvinylidene fluoride membranes (Millipore), incubated with specific antibodies and enhanced chemiluminescence (Amersham) was used for detection. The following primary antibodies were used: mouse monoclonal anti-c-Myc, mouse monoclonal anti-Cyclin D1, rabbit polyclonal anti-cyclin D2, goat polyclonal anti-MafB (Santa Cruz), rabbit polyclonal anti-p38 (Cell signaling), mouse monoclonal anti-Tata-binding protein (Tbp, EMD Millipore and Abcam).

QUANTIFICATION AND STATISTICAL ANALYSIS

Data are presented as mean ± SD. Sample number (n) indicates the number of independent biological samples in each experiment. Sample numbers and experimental repeats are indicated in figures and figure legends or methods section above. p value of datasets was determined by Student's t test with 95% confidence interval. All statistical tests were performed with Graph Pad Prism V4 software (*$p < 0.05$, **$p < 0.01$, ***$p < 0.001$, ****$p < 0.0001$, n.s. not significant).

DATA AVAILABILITY

The accession number for the gene array data reported in this paper is ArrayExpress: E-MTAB-5085. The accession number for the scRNA seq data reported in this paper is NCBI GEO: GSE86929.

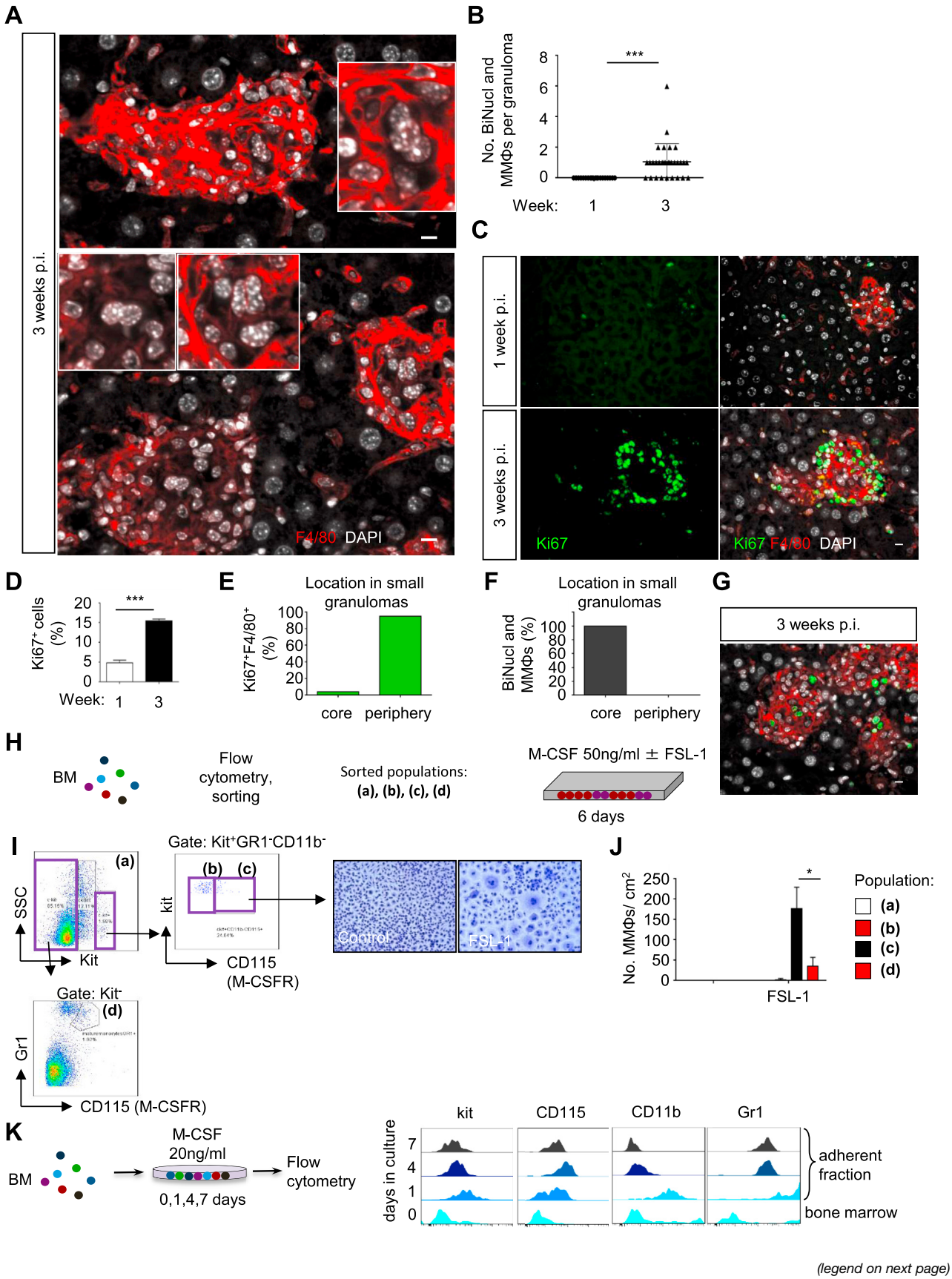

(legend on next page)

Figure S1. MΦ Precursors Rather than Differentiated Monocytes form MMΦs, Related to Figure 1

(A–G) C57BL/6 mice were infected with *Mycobacterium (M.) bovis* BCG *i.p*. and analyzed at the indicated time points.

(A) IF for F4/80 and DAPI in liver granulomas. p.i., post infection.

(B) Quantification of BiNucl and MultiNucl cells/granuloma. Mean ± SD from 3 mice per time point are shown.

(C) IF for F4/80, Ki67, DAPI in liver granulomas. p.i., post infection. Note the small size of granuloma nuclei associated with $F4/80^+$ cells 1 week after infection.

(D) Quantification of $Ki67^+$ MΦ by QIBC. Mean ± SD from 1300-4000 nuclei per mouse from 3 mice per time point shown as percent of total nuclei analyzed.

(E and F) Quantitation of the location of BiNucl and MMΦs and $Ki67^+F4/80^+$ cells in granulomas. 50 granulomas pooled from 3 mice infected with M. bovis BCG 3 weeks post infection were analyzed.

(G) Position of $Ki67^+F4/80^+$ cells in larger granulomas is ill-defined. Representative images of liver sections stained with antibodies to F4/80, Ki67 and DAPI are shown. p.i., post infection.

(H) Experimental set up related to Figures S1I and S1J.

(I) At the left, representative flow cytometric dot plots of bone marrow (BM), indicating the gates used to sort (a) whole BM, (b) uncommitted hematopoietic progenitors (identified as $Gr1^-CD11b^-Kit^+CD115^-$), (c) common macrophage dendritic cell progenitors (MDPs, identified as $Gr1^-CD11b^-Kit^+CD115^+$), and (d) mature monocytes ($Gr1^{int/-}CD11b^+Kit^-CD115^+$). At the right, representative pictures of sorted MDPs stimulated with FSL-1 versus medium for 6 days, then fixed and stained with Hemacolor (Sigma).

(J) Quantification of the number of MMΦs. The bars show mean ± SD of 3 independent experiments.

(K) Experimental set-up and representative flow cytometric histograms of BM and BM-derived mononuclear phagocytes. Whole BM was stained for flow cytometry directly (day 0) or adherent cells were harvested after 1, 3, 7 days of culture and stained for flow cytometry.

***$p < 0.001$, Scale Bars, 10 μm.

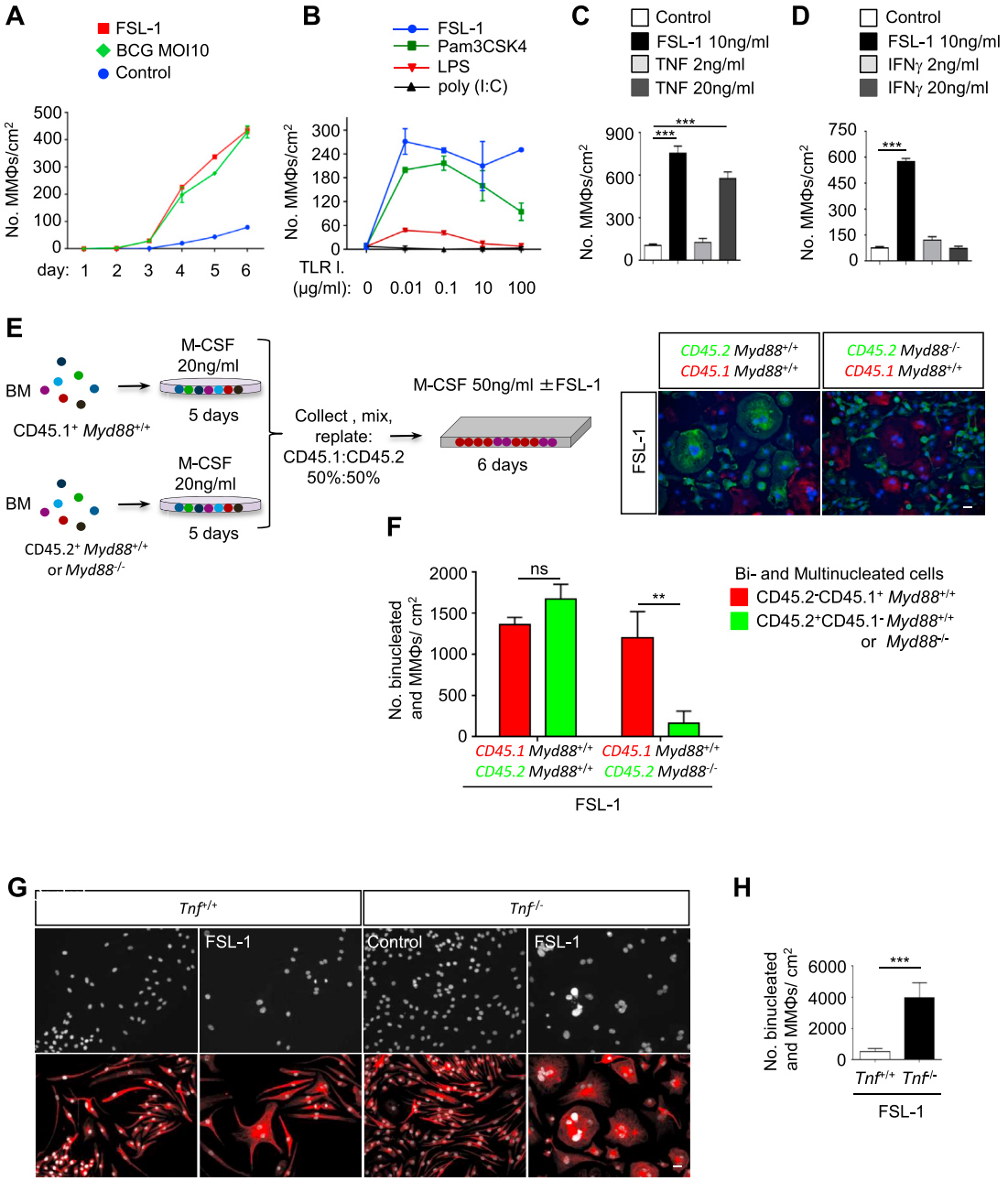

Figure S2. Identification of Inflammatory Signals Leading to MMΦ Formation, Related to Figure 1

(A) Quantification of MMΦ, as a timeline, following stimulation with FSL-1, BCG or medium. The bars show mean ± SD from 3 independent experiments.

(B–D) Identification of inflammatory signals leading to MMΦ formation. Quantification of MMΦ, following MΦ precursors stimulation with the indicated cytokines or TLR ligands. Data are shown as mean ± SD from 3 independent experiments.

(E and F) Requirement for MyD88 at the single cell level for TLR2-induced generation of MMΦ. A 1:1 mixture of CD45.1^{+}*Myd88*$^{+/+}$ and CD45.2^{+}*Myd88*$^{-/-}$ MΦ precursors were stimulated with FSL-1 (20ng/ml) or medium and MMΦ were analyzed for CD45.1 and CD45.2 expression. (E) Representative images of one out of 3 independent experiments are shown. (F) Quantification of CD45.1 and CD45.2 expression by MMΦ. Data are representative of 3 independent experiments.

(G and H) TNF is not required for TLR2-induced generation of MMΦ. *Tnf*$^{+/+}$ and *Tnf*$^{-/-}$ MΦ precursors were stimulated with FSL-1 for 6 days. (G) Representative images of one out of 2 independent experiments are shown. (H) Quantification of BiNucl and MMΦ in an unbiased, automated manner, by QIBC. The bars show mean ± SD from 2 independent experiments.

*** < 0.001, Scale Bars, 10 μm.

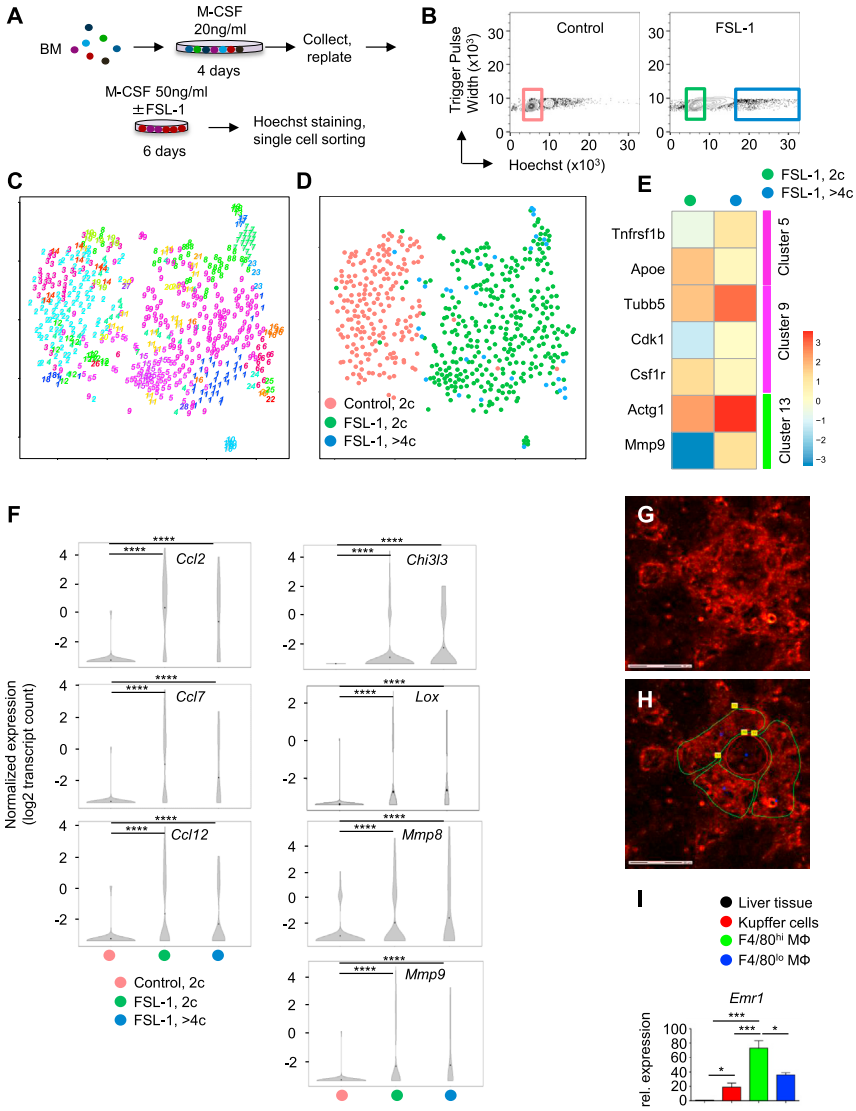

Figure S3. Gene Signatures Characteristic of Polyploid Macrophages, Related to Figure 1

(A) Experimental set up for scRNA-seq experiments (related to Figures 1H, 1K, 4B, S3C–S3F, and S4).

(B) Sorting strategy for scRNA-seq experiments. Doublets were excluded based on Trigger Pulse Width. Control MΦ precursors with a 2c DNA content and FSL-1 stimulated MΦ precursors with 2c (diploid) and > 4c (polyploid) DNA content were single cell sorted for RNA-seq.

(C) t-SNE map representation of transcriptome similarities of control 2c, FSL-1-stimulated 2c and > 4c macrophages. RaceID2 algorithm identified 28 different clusters including outliers, highlighted with different colors and numbers.

(D) t-SNE map showing the experimental condition for each cell.

(E) Heatmap showing the expression profile of shortlisted genes characterizing MMΦ differentiation in FSL-1-stimulated 2c and > 4c MMΦ within cluster 5, 9 and 13.

(F) Violin plots comparing expression of *Ccl2, Cll7, Ccl12* (C) and *Chi3l3, Lox, Mmp8* and *Mmp9* (D) in MΦ precursors stimulated with FSL-1 or medium for 6 days, isolated based on their DNA content and analyzed by single cell RNA-seq. The y axis indicates the log2 (normalized count+0.1) expression levels. The black point indicates the mean of expression level.

(G and H) C57BL/6 mice were infected with *Mycobacterium (M.) bovis* BCG *i.p.* 3 weeks post infection liver cryosections were stained with F4/80. Indicated populations were isolated by laser capture microdissection (LCM). Representative images of liver granuloma before LCM- (G) and after (H) LCM-guided isolation of F4/80^{hi} and F4/80^{low} bi- and multinucleated granuloma macrophages.

(I) qRT-PCR analysis of *Emr1* mRNA expression (encoding F4/80) in granuloma MΦ populations, liver Kupffer cells and liver tissue verifying purity of isolated populations. Data are shown as mean ± SEM of duplicate determinants from 5-9 independent biological replicates per group and are normalized relative to *Gapdh* mRNA expression.

*p < 0.05, *** < 0.001, Scale Bar 30 μm.

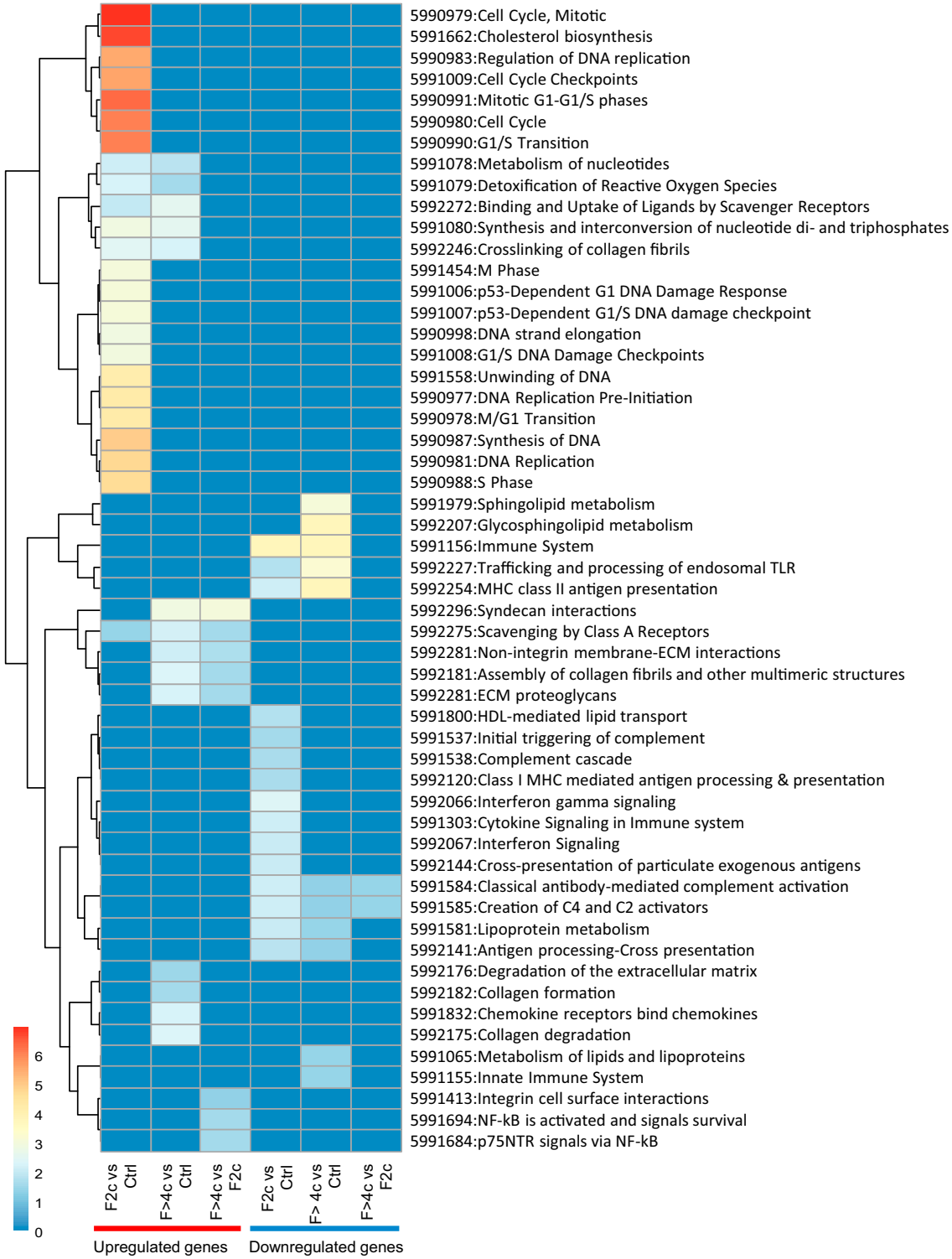

Figure S4. Gene Signatures Characteristic of Polyploid Macrophages-Reactome Pathway Enrichment Analysis, Related to Figure 1

MΦ precursors stimulated with FSL-1 or medium for 6 days were isolated based on their DNA content and analyzed by single cell RNA-seq. Reactome pathway enrichment analysis was performed on genes exhibiting a minimum of 2-fold expression difference between the two subgroups with a p-adjusted value less than 0.05.

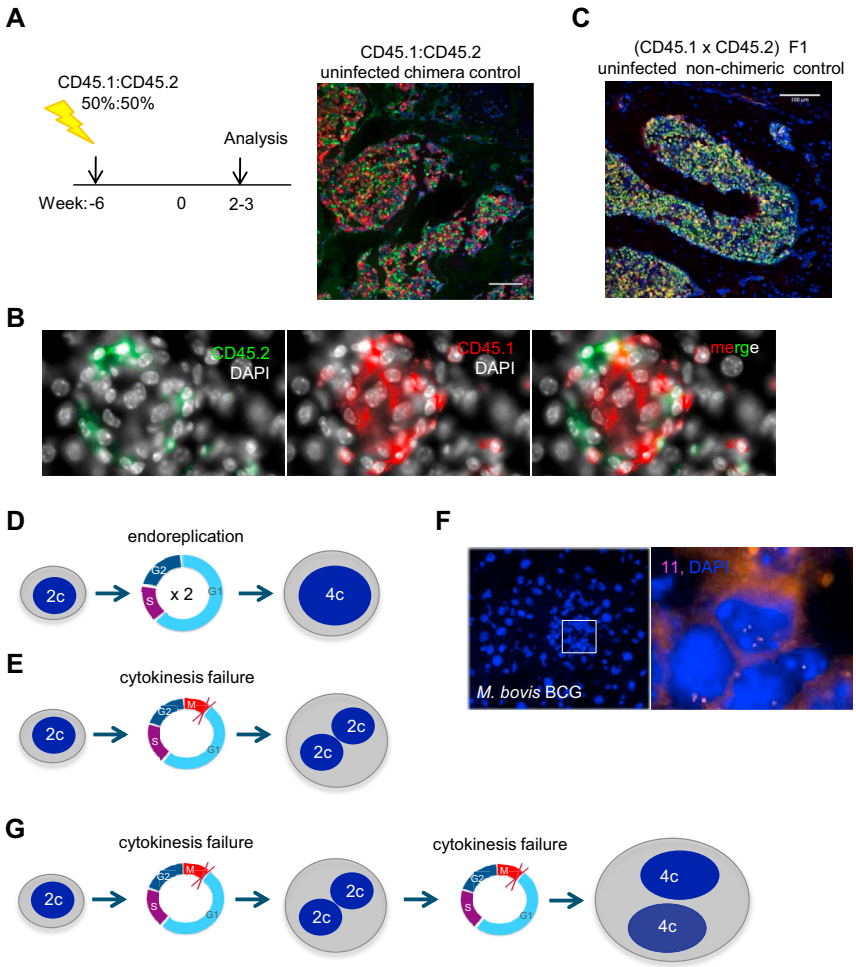

Figure S5. MMΦ Formation from MΦ Precursors Does Not Involve Cell-to-Cell Fusion, Related to Figure 2

(A and B) *M. bovis* BCG-induced MMΦ do not require cell-to-cell fusion in vivo. (A) CD45.2 mice were lethally irradiated and reconstituted with a mixture of BM cells from CD45.1 and CD45.2 mice. 6-12 weeks later, uninfected mice were analyzed. Representative images of bone cryosections from 2 independent experiments showing roughly equal numbers of either $CD45.1^+$ or $CD45.2^+$ bone marrow leukocytes. Scale Bar 100 μm

(B) CD45.2 mice were lethally irradiated and reconstituted with a 1:1 mixture of bone marrow cells from CD45.1 and CD45.2 mice. 6-12 weeks later, the mice were infected with *M. bovis* BCG *i.p.* and analyzed 2-3 weeks p.i. Liver granuloma cryosections were stained with antibodies to CD45.1, CD45.2 and F4/80. Representative images from 3 independent experiments with n = 5 mice per experiment are shown. p.i., post infection.

(C) (CD45.1xCD45.2)F1 non-chimeric uninfected mice were analyzed as controls. Representative images of bone cryosections from 2 independent experiments showing numerous leucocytes double positive for CD45.1 and CD45.2. Scale Bar 100 μm

(D) Schematic depiction of polyploidy arising via endoreplication: cycling cells undergo multiple cell cycles without entering mitosis, doubling their DNA content within a single nucleus.

(E) Schematic depiction of polyploidy arising via cytokinesis failure: cells enter mitosis but fail to physically split into two following chromosome segregation, giving rise to BiNucl tetraploid daughter cells.

(F) C57BL/6 wild-type were infected with *M. bovis* BCG *i.p.* 2-3 weeks p.i. liver cryosections were analyzed by FISH for chromosome 11. Representative pictures from 3 independent experiments are shown. p.i., post infection.

(G) Schematic depiction of polyploidy arising via cytokinesis failure: following a first cytokinesis failure, BiNucl tetraploid daughter cells, re-enter mitosis and re-distribute their genetic content into two nuclei thus generating a BiNucl daughter cell with 4c DNA content in each nucleus.

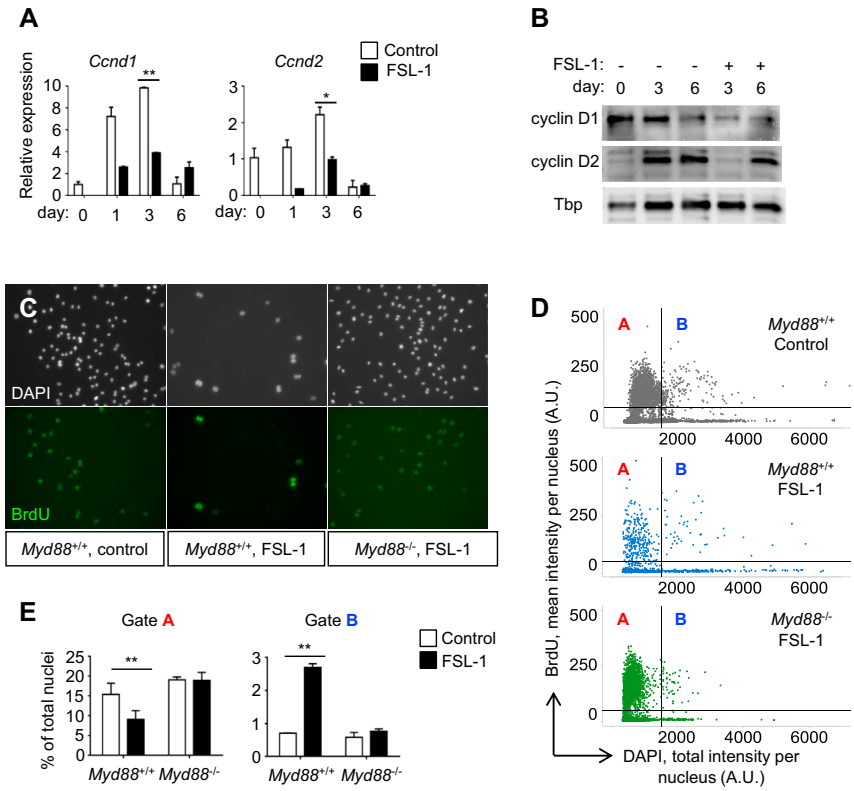

Figure S6. TLR2 Signaling Confers a Proliferation Advantage to Polyploid MΦ Progeny, Related to Figure 4

(A) qRT-PCR of *Cnnd1 and Cnnd2* mRNA, normalized relative to *Gapdh* mRNA expression. Mean ± SD of triplicate determinants pooled from 3 independent experiments.

(B) IB of nuclear lysates for Cyclins D1 and D2. Example of 2 independent experiments.

(C–E) Increased BrdU incorporation into polyploid nuclei, IF for BrdU, DAPI; QIBC. (C) Representative images. (D) Mean BrdU fluorescence versus total DAPI intensity per single nucleus. (E) Percent of $BrdU^+$ nuclei belonging in gate A or B, as in (D). n = 1000-5000 nuclei per condition. Mean ± SD from 3 independent experiments.

*p < 0.05, **p < 0.01, Scale Bar, 10 μm.

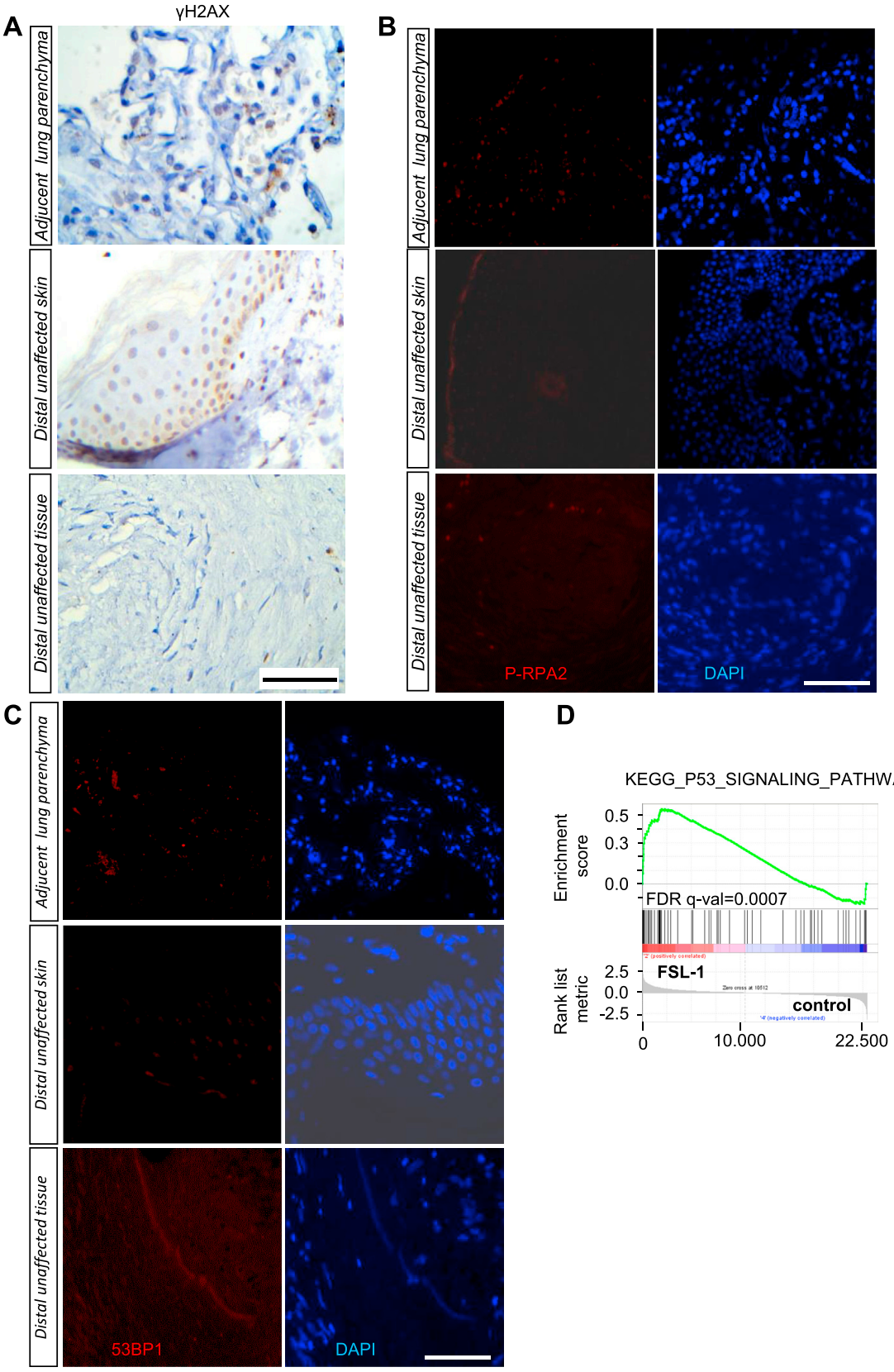

(legend on next page)

Figure S7. Replication Stress and Activated DDR in Granulomas Enriched in MMΦ In Vivo, Related to Figure 6

(A–C) Representative images of uninvolved tissue adjacent from granulomatous areas from 10-15 patient biopsies per granulomatous disease are shown. (A) IH for γH2AX. (B) IF for p-RPA2. (C) IF for 53BP1. n = 10-17 patient biopsies per disease.

(D) GSEA for p53-dependent genes in MΦ precursors stimulated for 6 days with FSL-1 versus medium. Gene array was performed with 4 independent biological replicates per group.

Scale Bars, 100 μm.